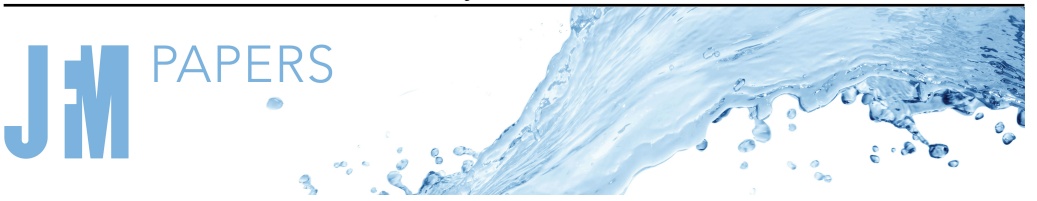
J. Fluid Mech. (2025), *vol.* 1019, A26, doi:10.1017/jfm.2025.10590



On the freely falling circular cylinder with a splitter plate

Yue-Hao Sun[1,2], **Yi-Ming Huang**[1,2] **and Zhen Chen**[1,2]

[1]Marine Numerical Experiment Center, State Key Laboratory of Ocean Engineering, Shanghai 200240, PR China

[2]School of Ocean and Civil Engineering, Shanghai Jiao Tong University, Shanghai 200240, PR China

Corresponding author: Zhen Chen, zhen.chen@sjtu.edu.cn

(Received 12 October 2024; revised 5 August 2025; accepted 15 August 2025)

In this paper, a freely falling circular cylinder attached by a splitter plate in an infinite fluid domain under gravity is investigated numerically. The kinematic modes and wake patterns are summarised, and their parametric sensitivity with the dimensionless plate length (L^*), the Galileo number (Ga) and the cylindric-fluid density ratio (ρ^*) is studied. The kinematic modes of a freely falling circular cylinder with a splitter plate can be classified into six types: the steady falling, the steady oblique falling, the small vibration oblique falling, the zigzag oblique falling, the locked falling and the chaotic falling. In the meantime, the wake patterns can be summarised into five types: the steady wake, the 2S wake, the 2P + nS wake, the 2P + 2S wake, and the chaotic wake. The effect of the length of the splitter plate on the vortex shedding characteristics represented by the Strouhal number is also discussed. Further investigation reveals that the attachment of a splitter plate of different lengths to the rear not only influences the kinematic mode and the vortex shedding of the circular cylinder, but also allows the passive and precise control of its falling posture and trajectory. Finally, through theoretical analysis, scaling laws are proposed to estimate the turn angle α and the drift angle β. The present study can deepen the understanding of similar natural phenomena, such as gliding birds and falling maple seeds, and provide valuable reference for engineering design of drag-reduction devices or air-dropped objects.

Key words: flow-structure interactions, vortex shedding

1. Introduction

Natural organisms have evolved a variety of morphologies and structural features towards drag reduction and lift generation, and thus enhanced agility. Examples include the tubercles of a humpback whale flipper (Fish & Lauder 2006), deformable feathers of birds (Favier *et al.* 2009), and the wind-dispersed seeds of maple and dandelion (Lentink

© The Author(s), 2025. Published by Cambridge University Press.

https://doi.org/10.1017/jfm.2025.10590 Published online by Cambridge University Press

et al. 2009; Cummins *et al.* 2018). These examples can be categorised into the passive flow control strategy, which refers to the way of modifying the ambient flow field without consuming energy (Fish & Lauder 2006). The natural selection of these elegant structures could inspire technological innovation of human applications.

A common approach of passive flow control is to attach a splitter plate to the rear of a circular cylinder, the effectiveness of which depends on the specific problem being addressed. The present section provides a concise review of previous research on splitter plates, and elucidates the rationale behind this study. For a stationary circular cylinder in uniform flow, flow separation occurs in a wide range of Reynolds numbers, which may incur Kármán vortices and thus oscillatory drag and lateral forces on the circular cylinder (Williamson 1996). Roshko (1954) reported a pioneering experimental discovery that a rigid splitter plate fixed downstream of the circular cylinder could inhibit the formation and shedding of vortices, which favours the drag reduction. Subsequently, several studies (Apelt, West & Szewczyk 1973; Kwon & Choi 1996) have investigated this phenomenon more systematically. These results reveal more clearly the wake characteristics after a circular cylinder with a splitter plate, which reduces the Strouhal number to some degree. A flexible splitter plate hinged behind the circular cylinder leads to another interesting phenomenon, spontaneous symmetry breaking, which was observed by Bagheri, Mazzino & Bottaro (2012) and leads to the generation of net lift.

The elastically mounted circular cylinder interacting with incoming flows could show more complicated kinematics that is usually termed the vortex-induced vibration (VIV). Attachment of the splitter plate in such scenario may help to stabilise the circular cylinder, which was first reported by Assi, Bearman & Kitney (2009). Later studies discussed the range of parameters over which the VIV amplitude is suppressed, including the configurations of a hinged flexible splitter plate (Wu *et al.* 2014) and a rigid splitter plate with rigid connection (Sun *et al.* 2020). More recently, Muñoz-Hervás *et al.* (2024) demonstrated through experiments that the hinged flexible plate can attenuate the response of the VIV system by altering the shedding frequency.

The circular cylinder may exhibit more complicated kinematics when the rotational degree of freedom is released. In such circumstances, the attachment of the splitter plate could bring abundant variation into this fluid–structure interaction (FSI) system. Cimbala and his co-workers carried out a series of experiments on this issue (Cimbala & Garg 1991; Cimbala & Chen 1994; Cimbala & Leon 1996), and found that in a broad range of Reynolds numbers, the rotatable circular cylinder with a splitter plate would stabilise at a certain angle in a uniform flow, which is a phenomenon of symmetry breaking. This phenomenon was numerically confirmed by Xu, Sen & Gad-el Hak (1990), who also reported the threshold Reynolds number for the circular cylinder to initiate rotation, and its correlation to the length of the splitter plate. The experiments conducted by Gu *et al.* (2012) on a rotatable circular cylinder with a splitter plate revealed that for smaller plate length, the separation flow would reattach to the plate, whereas for a longer plate, the reattachment may not occur. Through linear stability analysis, Basso *et al.* (2021) and Jiang *et al.* (2025) determined that the source of the instability of the symmetry breaking is related to the flow field near the splitter plate.

A more complicated configuration of this category of problem would be the FSI of a freely falling object. Early explorations were focused on the freely falling/rising two-dimensional circular cylinder or three-dimensional sphere, as well as associated physical problems such as the sedimentation process. Specifically, Namkoong *et al.* (2008) discussed the discrepancy in vortex shedding frequency between the fixed circular cylinder and the freely falling/rising circular cylinder. The experimental studies done by Jenny, Duek & Bouchet (2004) and Horowitz & Williamson (2010) reported a variety

https://doi.org/10.1017/jfm.2025.10590 Published online by Cambridge University Press

of oscillatory rising/falling motions of a sphere. Besides, Horowitz & Williamson (2010) summarised four typical modes of motion for a freely falling/rising sphere over a wide range of parameters (namely, vertical, oblique, intermittent oblique and zigzag), and three modes of vortex shedding (namely, 'R', '2R' and '4R', where 'R' represents the vortex ring). The role of splitter plates in modifying the FSI dynamics of typical geometries such as the circular cylinder or the sphere has been explored in previous studies under certain constraints of freedom (Lācis *et al.* 2014, 2017). Building on this, Choi *et al.* (2025) recently conducted experiments on a similar model – a freely falling sphere with a rigid filament. They observed that the filament induced a distinct periodic zigzag motion by causing the sphere to rotate at the Reynolds number of $O(10^3)$, while the long filament ($L/D = 3.0$) could be observed by the readers to have an inclined settling trajectory. These works revealed that splitter plates could induce asymmetric posture, leading to stable inclined trajectories and rotational equilibrium phenomena. But these studies imposed strong constraints: limited degrees of freedom were endowed to the motion of the structure in some of the previous works, and the range of the parameters considered was narrow. These simplifications ignored the effects of gravity and viscosity, and left an open question of how the splitter plates modulate the complex falling trajectories. Consequently, the role of the splitter plates in altering the falling posture and trajectory stability remains unclear, and the parametric guidelines for effective control have not yet been established.

In recognition of the research gap such that most existing works have been focused on the role of the splitter plate in reducing drag and suppressing oscillation amplitude, this study will explore its effects in regulating the posture and the trajectory of a truly freely falling body with no constraints. By simulating a circular cylinder attached by a splitter plate in an infinite fluid domain, this study will present more abundant details of the fluid–structure interplay, and investigate how the splitter plate mediates transitions between different kinematic modes and wake patterns. This work redefines the splitter plate as an effective trajectory stabiliser of the freely falling bodies. By integrating the influences of the plate length, gravity and viscous damping, the force equilibrium relationship is proposed, based on which the prediction formulations of the turn angle and the drift angle are established. The kinematics in this work could be correlated with natural systems (e.g. maple seeds, avian gliding) and engineering applications (e.g. underwater gliders, air-dropped objects), which advances the fundamental understanding and provides valuable insights into the passive control strategy for freely falling objects.

The remainder of this paper is organised as follows. The physical problem and the numerical method are described in § 2 and Appendix A. The results and discussions are presented in § 3. Finally, concluding remarks are given in § 4.

2. Computational model

2.1. *Physical problem*

The physical configuration of the problem studied is shown in figure 1. The circular cylinder with a rigidly connected splitter plate is placed in the static fluid, and the centre of the circular cylinder is set as the origin point of the coordinates. The structure is released from an initial state of rest at the initial time, then undergoes motions with three degrees of freedom under the influence of gravity. The computational domain is dynamically adjusted via the arbitrary Lagrangian–Eulerian (ALE) method to maintain the cylinder at the origin, which allows the efficient simulation of the free falling of the circular cylinder in an infinite fluid domain. Boundary conditions include the Dirichlet boundary condition (zero uniform inlet velocity) at the bottom, and the Neumann boundary conditions (zero traction) on

https://doi.org/10.1017/jfm.2025.10590 Published online by Cambridge University Press

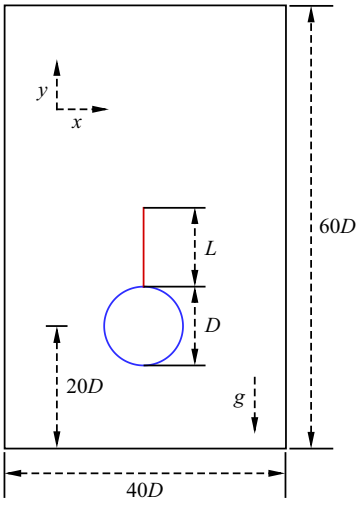


Figure 1. Schematic diagram for the circular cylinder with a splitter plate. The circular cylinder with diameter D is placed in a static flow initially. The splitter plate with length L, parallel to the gravitational acceleration g initially, is rigidly connected to the rear of the circular cylinder.

all other boundaries. The geometric characteristic of this structure is described by the dimensionless parameter $L^* = L/D$, where L and D are the length of the splitter plate and the diameter of the circular cylinder, respectively. It is noteworthy that $L^* = 0$ refers to the case without the splitter plate.

The problem investigated here calls for the resolution of the fluid and the structure. Specifically, the incompressible fluid behaviour can be described by the Navier–Stokes equations in a weakly compressible form

$$\frac{\partial \rho}{\partial t} + \nabla \cdot \rho \boldsymbol{u} = 0, \tag{2.1}$$

$$\frac{\partial \rho \boldsymbol{u}}{\partial t} + \nabla(\rho \boldsymbol{u}\boldsymbol{u}) = -\nabla p + \nabla \cdot \left[\mu \left(\nabla \boldsymbol{u} + (\nabla \boldsymbol{u})^{\mathrm{T}}\right)\right] + \boldsymbol{f}, \tag{2.2}$$

where $\boldsymbol{u}$ is the fluid velocity, ρ is the density of the fluid, p is the pressure, μ is the dynamic viscosity, and $\boldsymbol{f}$ is the body force term.

The motion of the circular cylinder with the splitter plate can be described by the Newton–Euler equations at the centre of mass:

$$M\frac{\mathrm{d}\boldsymbol{U}}{\mathrm{d}t} = -M\left(1 - \frac{\rho}{\rho_s}\right)\boldsymbol{g} + \boldsymbol{F}, \tag{2.3}$$

$$I\frac{\mathrm{d}\omega}{\mathrm{d}t} = T_Z, \tag{2.4}$$

where M and I are the mass and the moment of inertia of the structure, respectively, $\boldsymbol{U}$ and ω are the translational velocity and the angular velocity of the structure, respectively, ρ_s is the density of the circular cylinder, $\boldsymbol{g}$ is the acceleration due to gravity, and $\boldsymbol{F}$ and T_Z are, respectively, the force and the torque on the structure. The circular cylinder is solid with mass $\rho_s \pi D^2/4$ and moment of inertia $\rho_s \pi D^4/32$, while the splitter plate is considered as a thin plate of mass m_p and moment of inertia $m_p L^2/12$. From this, the position of the centre of mass and the moment of inertia at the centre of mass can be calculated. It is noteworthy that the thickness of the splitter plater is ignored as in previous studies (Huang,

https://doi.org/10.1017/jfm.2025.10590 Published online by Cambridge University Press

Shin & Sung 2007; Peng *et al.* 2022; Sun *et al.* 2022). The effect of the mass of the splitter plate is discussed in § 3.2. In most of the cases studied here, zero plate mass is employed.

The dimensionless group of this study includes the normalised plate length L^*, the density ratio $\rho^* = \rho_s/\rho$, the Galileo number $Ga = \sqrt{(\rho^* - 1)gD^3}/\nu$, and the Reynolds number $Re = U_{ref}D/\nu$, where $\nu = \mu/\rho$ and U_{ref} represent the kinematic viscosity and the mean falling velocity of the circular cylinder, respectively. The diameter of the cylinder is $D = 1\,\mathrm{cm}$, the density of the fluid is $\rho = 1\,\mathrm{g\,cm^{-3}}$, and the gravitational acceleration is $g = 980\,\mathrm{cm\,s^{-2}}$. The pressure coefficient is calculated in the form used by Namkoong *et al.* (2008),

$$C_p = \frac{p - p_s}{0.5\rho U_{ref}^2} + 1, \tag{2.5}$$

where p_s is the stagnation pressure, and U_{ref} is the average velocity of the circular cylinder. The definitions of force coefficients and the torque coefficient are $C_L = F_X/0.5\rho U_{ref}^2 D$, $C_D = F_Y/0.5\rho U_{ref}^2 D$ and $C_T = T_z/0.5\rho U_{ref}^2 D^2$, where F_X and F_Y are the horizontal and vertical components of the forces on the structure, respectively, and T_z is the torque induced by the force on the strucutural surface about the centre of the circular cylinder. Further details of the numerical method employed in the present study are in Appendix A.

2.2. *Validation*

Validation of the numerical method employed in this study is carried out by considering a freely falling circular cylinder in the infinite flow field with $\rho^* = 1.01$, $Ga = 138$, $L^* = 0.0$. Figure 2(*a*) compares the horizontal, vertical and angular velocities (U_C, V_C and ω_C) obtained by the present method and the reference results of Namkoong *et al.* (2008). The vertical velocity fluctuates around $V_C = 2.5\,\mathrm{cm\,s^{-1}}$. As shown in the inset of figure 2(*a*), the small fluctuation is well captured by the present solver, which demonstrates the accuracy of the numerical method employed.

To further validate the numerical method, the rotatable circular cylinders with four different lengths of splitter plate are numerically simulated in the condition $Re = 160$ (see figure 2*b*). In these cases, the centre of the circular cylinder is fixed, but the rotational degree of freedom is released. Compared with previous studies (Cimbala & Garg 1991; Assi *et al.* 2009; Tang *et al.* 2022), the present results show good consistency.

Further validation of the numerical method is carried out by comparing with the experimental data of a freely falling plate in Andersen *et al.* (2005). The aspect ratios of the plate are 1 : 5 and 1 : 14, and the Reynolds numbers are $Re = 737$ and $Re = 1147$, respectively. As shown in figure 2(*c*) and table 1, the falling motion and the averaged velocities obtained by the present numerical method show good agreement with the experimental results.

In order to verify the correctness of the calculations, a series of tests has been carried out regarding the configuration of a freely falling circular cylinder with a splitter plate. Independence studies of the domain size, the mesh spacing, the artificial Mach number, and the time step dt, are performed, as shown in table 2. In the following simulations, d$h = 0.01$ and d$t = 0.005$ are used to ensure convergence of the calculation. The computational domain of the fluid field is set as $40D \times 60D$, which is sufficiently large to render the impact of the boundary on the numerical results. The near-structure region $[-2.6D, 2.6D] \times [-0.6, 1.6D + L]$ is discretised by the fine mesh spacing d$h =$ 0.01, while the far field is discretised with stretched meshes to reduce computational effort. An independence study of the Lagrangian mesh spacing is also carried out, as shown in figure 3(*a*), which implies that the Lagrangian mesh spacing $\Delta l = 0.02D$ is sufficient to

https://doi.org/10.1017/jfm.2025.10590 Published online by Cambridge University Press

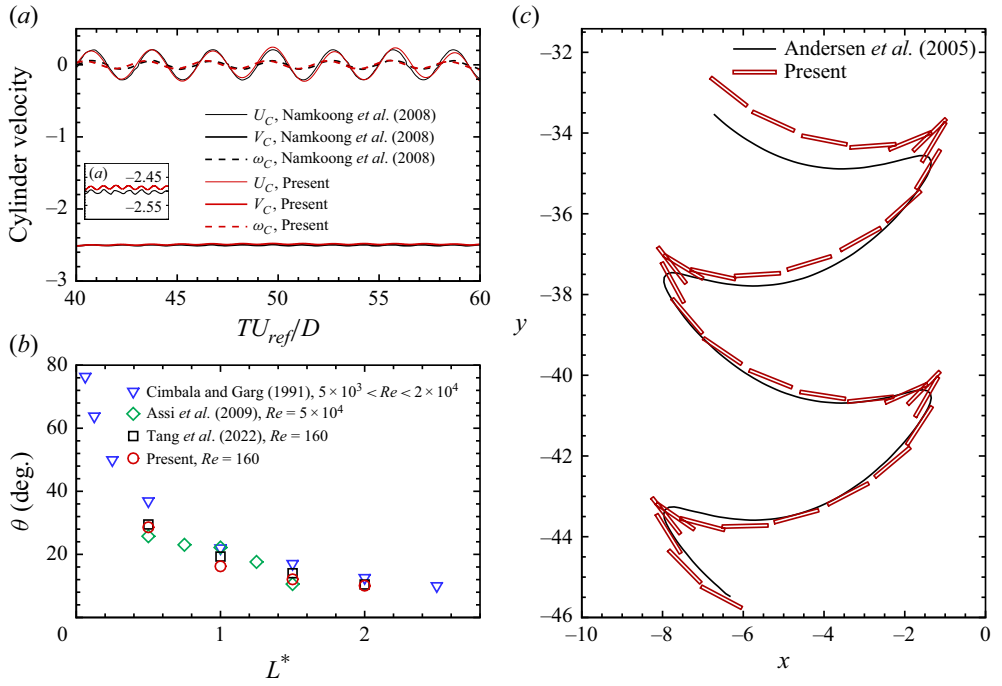


Figure 2. Validations of the present numerical method. (*a*) Time histories of the velocity of a freely falling circular cylinder, and their comparisons with the results of Namkoong *et al.* (2008). In this case, $\rho^* = 1.01$, $Ga = 138$, $L^* = 0.0$. Note that the fluctuation of V_c is small and fluctuates around $V_c = 2.5$ cm s^{-1}, which is shown in the inset. (*b*) The mean rotation angle (θ) of a rotatable circular cylinder with a splitter plate of different lengths L^* in the uniform flow and its comparison with the reference data (Cimbala & Garg 1991; Assi *et al.* 2009; Tang *et al.* 2022). Here, $Re = 160$, $L^* = 0.5{-}2.0$. (*c*) The trajectory of a freely falling plate flutter in fluid at $Re = 1147$, comparing with the experiment of Andersen, Pesavento & Wang (2005).

Aspect ratio	Re	References	U_x (cm s^{-1})	V_y (cm s^{-1})	ω (rad s^{-1})	Motion
1 : 5	737	Andersen *et al.* (2005)	14.2 ± 0.1	-8.1 ± 0.3	25.5 ± 0.3	Tumbling
		Present	14.6	−7.9	25.3	Tumbling
1 : 14	1147	Andersen *et al.* (2005)	19.8 ± 0.3	-9.0 ± 0.2	6.8 ± 0.1	Fluttering
		Present	20.2	−9.0	6.9	Fluttering

Table 1. Comparison of translational (U_x and V_y) and angular (ω) velocities with experiment for the freely falling plate with different aspect ratios.

ensure numerical accuracy while reducing computational effort. Finally, the effect of the initial angle of attack is examined, as shown in figure 3(*b*). It is evident that the variation of the initial angle of attack does not alter the kinematics of the freely falling circular cylinder with a splitter.

3. Results and discussions

The validated numerical method is applied in this section for the study of the freely falling circular cylinder with a splitter plate in the infinite static fluid. Consistent with previous studies (Namkoong *et al.* 2008), the freely falling bare circular cylinder ($L^* = 0.0$)

https://doi.org/10.1017/jfm.2025.10590 Published online by Cambridge University Press

Calculation domain	dh	dt	Ma	St	α	β	C_D	$C_{L,rms}$
$25D \times 40D$	0.01	0.005	0.0608	0.1529	12.1265	5.9504	1.2512	0.0396
$40D \times 60D$	0.01	0.005	0.0612	0.1515	12.1614	6.3654	1.2334	0.0405
$60D \times 90D$	0.01	0.005	0.0614	0.1510	12.1890	6.5243	1.2265	0.0398
$40D \times 60D$	0.005	0.0025	0.0613	0.1522	12.4335	6.3102	1.2309	0.0412
$40D \times 60D$	0.01	0.005	0.0612	0.1515	12.1614	6.3654	1.2334	0.0405
$40D \times 60D$	0.02	0.01	0.0606	0.1491	11.8197	6.4664	1.2597	0.0406
$40D \times 60D$	0.01	0.0025	0.0612	0.1515	12.1579	6.3658	1.2337	0.0405
$40D \times 60D$	0.01	0.005	0.0307	0.1512	11.9662	6.4520	1.2229	0.0394
$40D \times 60D$	0.01	0.005	0.0612	0.1515	12.1614	6.3654	1.2334	0.0405
$40D \times 60D$	0.01	0.005	0.1217	0.1512	12.5057	6.2159	1.2471	0.0401
$40D \times 60D$	0.01	0.0075	0.0612	0.1514	12.1644	6.3654	1.2332	0.0406

Table 2. Numerical results for the Strouhal number St, the turn angle α, the drift angle β, the drag coefficient C_D, and the root mean square of the lift coefficient $C_{L,rms}$, obtained by set-ups with different domain sizes, mesh spacing dh, time step dt, and artificial Mach number Ma, for the case with $\rho^* = 1.01$, $Ga = 100$, $L^* = 1.0$.

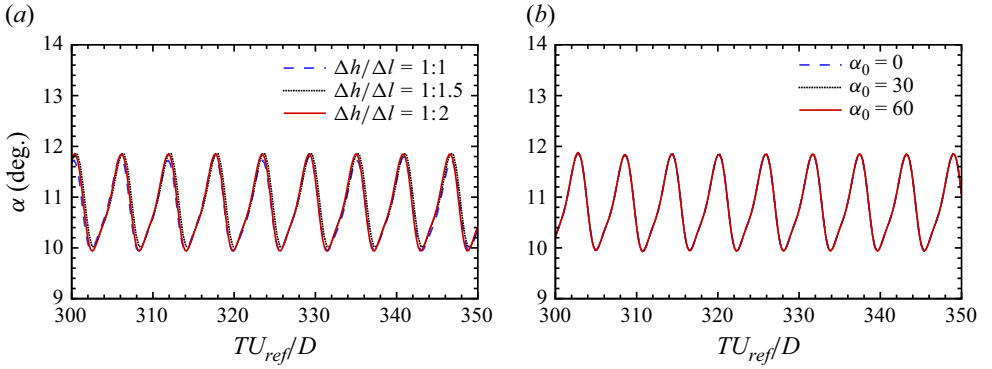


Figure 3. Independence study for the case with $\rho^* = 1.01$, $Ga = 150$, $L^* = 1.0$. (a) Independence study of the Lagrangian mesh spacing Δl, with fixed Eulerian mesh spacing $\Delta h = 0.01D$. (b) Independence study of the initial angle of attack α_0.

quickly reaches a stable state after an initial acceleration phase, settling into a primarily vertical trajectory with small amplitude of transverse oscillations. In contrast, attaching a splitter plate fundamentally alters this behaviour, often leading to the significant oblique trajectories that will be detailed in the following subsections. Comprehensiveness of the study is established by considering quite a wide range of dimensionless parameters, including the length of the splitter plate ($0.5 \leqslant L^* \leqslant 2.0$), the Galileo number ($25 \leqslant Ga \leqslant 800$), and the density ratio of the circular cylinder to the fluid ($1.01 \leqslant \rho^* \leqslant 2.60$).

3.1. *Kinematic states*

In this subsection, a summary and categorisation of the phenomena identified in the calculations will be presented. In the range of dimensionless paramenters mentioned above, the freely falling circular cylinder with a splitter plate exhibits six typical kinematic modes, namely the steady falling (SF), the steady oblique falling (SOF), the small vibration

https://doi.org/10.1017/jfm.2025.10590 Published online by Cambridge University Press

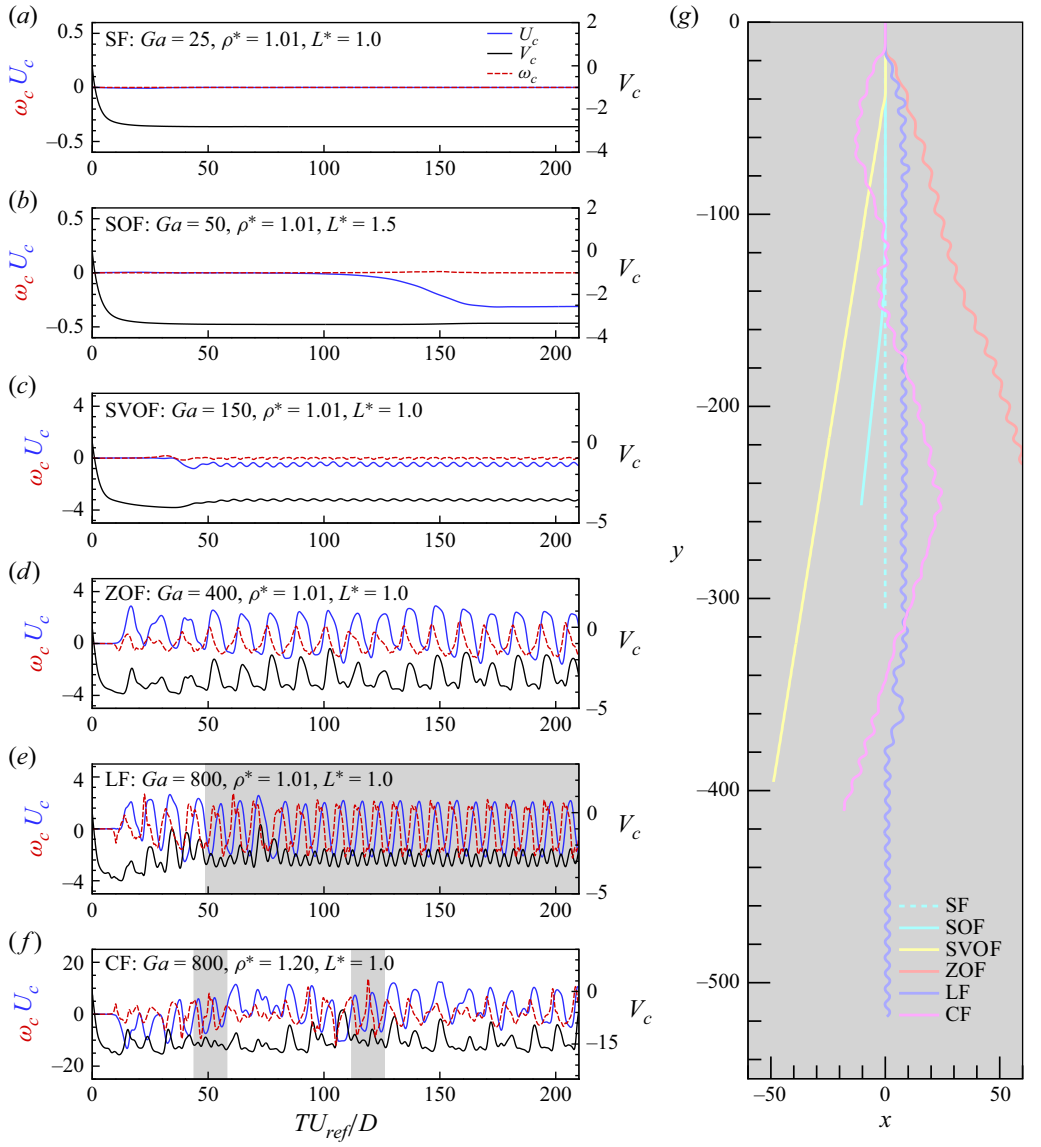


Figure 4. (*a–f*) Time histories of the velocities U_C (cm s^{-1}), V_C (cm s^{-1}) and ω_C (deg s^{-1}) for typical cases: (*a*) SF ($Ga = 25$, $\rho^* = 1.01$, $L^* = 1.0$), (*b*) SOF ($Ga = 50$, $\rho^* = 1.01$, $L^* = 1.5$), (*c*) SVOF ($Ga = 150$, $\rho^* = 1.01$, $L^* = 1.0$), (*d*) ZOF ($Ga = 400$, $\rho^* = 1.01$, $L^* = 1.0$), (*e*) LF ($Ga = 800$, $\rho^* = 1.01$, $L^* = 1.0$) and (*f*) CF ($Ga = 800$, $\rho^* = 1.20$, $L^* = 1.0$). (*g*) A general overview of the trajectory of a freely falling circular cylinder with a splitter plate at typical modes of kinematics.

oblique falling (SVOF), the zigzag oblique falling (ZOF), the locked falling (LF) and the chaotic falling (CF).

Figure 4 illustrates typical cases exhibiting the kinematic modes mentioned above. The distinct features of these modes are described as follows.

(i) Steady falling (SF): the circular cylinder reaches a steady state of vertical falling.
(ii) Steady oblique falling (SOF): the circular cylinder reaches a steady state of falling with unanimous non-vertical velocity. The symmetry breaking feature emerges.

https://doi.org/10.1017/jfm.2025.10590 Published online by Cambridge University Press

(iii) Small vibration oblique falling (SVOF): the circular cylinder exhibits an oblique falling trajectory, accompanied by a periodic transverse motion with small amplitude.
(iv) Zigzag oblique falling (ZOF): the circular cylinder shows an oblique falling trajectory and a transverse oscillation with considerable amplitude. The motion becomes increasingly disordered as Ga grows. This zigzag-shape motion with large amplitude of transverse motion was also found in studies of freely falling/rising spheres (Jenny *et al.* 2004; Horowitz & Williamson 2010).
(v) Locked falling (LF): the freely falling circular cylinder first follows the ZOF kinematic mode, then goes back to the vertical falling mode with better periodicity, such as the grey background region illustrated in figure 4(*e*). A similar phenomenon was also identified in experiments of freely falling/rising spheres (Jenny *et al.* 2004) and freely falling shperes with a rigid filament (Choi *et al.* 2025).
(vi) Chaotic falling (CF): the motion of the circular cylinder exhibits a more chaotic behaviour. The direction of the oblique falling trajectory may be altered after an intermittent motion of the LF modes (see the grey background regions in figure 4*f*). A similar phenomenon was also recognised by Jenny *et al.* (2004).

In the following subsubsections, thorough discussions of each kinematic mode will be presented, together with a summary of the wake patterns.

3.1.1. *The SF and SOF modes*

As summarised at the start of § 3.1, the falling trajectory of the circular cylinder with a splitter plate is typically a straight vertical or oblique line (see figure 4*g*), corresponding to the SF or SOF mode, respectively. Time histories of the velocities (U_C, V_C and ω_C) of the circular cylinder shown in figures 4(*a*) and 4(*b*) indicate the evolution towards a steady rate of falling. In contrast to the SF mode, a non-zero horizontal velocity $U_C = -0.3083$ cm s^{-1} is presented in the present example exhibiting the SOF mode of kinematics.

Figure 5 presents the vorticity contours and the pressure distributions on the structure for the two typical cases, where Θ is the angular coordinate of the circular cylinder, and y is the coordinate on the plate; here, $\Theta = \pm 180°$ or $y = 0$ represents the junction point between the splitter plate and the circular cylinder. It can be seen that for the SF mode, the steady wake is formed in the downstream of the circular cylinder. Shear layers with opposite vorticities are formed on the two sides of the circular cylinder, then vanish due to the dissipation. However, for the SOF mode, the circular cylinder with a splitter plate exhibited the symmetry breaking phenomenon during falling, manifesting as the rotation to turn angle $\alpha = 5.5869°$ and the inclined falling trajectory at drift angle $\beta = 5.2826°$. The motion of the SOF mode represents a state that exceeds the Reynolds number of critical equilibria (Xu *et al.* 1990), but remains under the threshold Reynolds number of vortex shedding. Essentially, it is the flow instability that attracts the splitter plate to one side and thus breaks symmetricity about the vertical coordinate. Figure 5(*b*) shows the asymmetric pressure distribution on the structure, while the angular position of the stagnation point on the circular cylinder approximately locates at $\Theta = 18°$.

3.1.2. *The SVOF mode*

With increased values of Ga, vortex shedding occurs, which leads to small vibrations in the velocities of the circular cylinder with a splitter plate (see figure 4*c*). Figure 6 illustrates the kinematic characteristics of the SVOF mode with the case of $Ga = 150$, $\rho^* = 1.01$ and $L^* = 1.0$. It is evident that the turn angle α shows periodic fluctuations with amplitudes within 2°. Furthermore, C_T exhibits two extremely large peaks of different sizes in one

https://doi.org/10.1017/jfm.2025.10590 Published online by Cambridge University Press

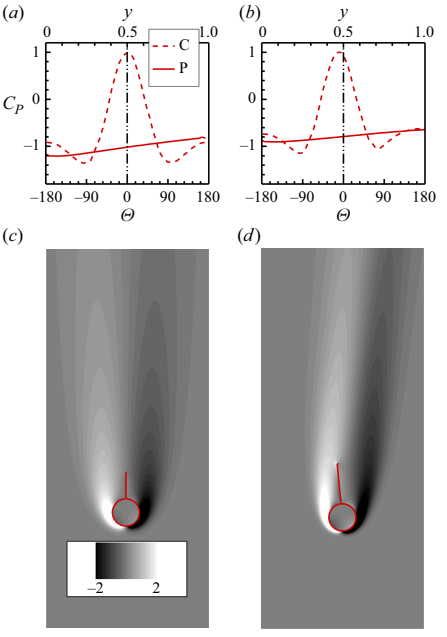


Figure 5. Vorticity contours (*c*,*d*) and the corresponding pressure distributions on the structure (*a*,*b*) for typical cases: (*a*,*c*) SF, $Ga = 25$, $\rho^* = 1.01$, $L^* = 0.5$; (*b*,*d*) SOF, $Ga = 50$, $\rho^* = 1.01$, $L^* = 1.5$. The red dashed lines and the solid lines in (*a*,*b*) represent the pressure distributions on the circular cylinder (C) and on the plate (P), respectively. The black dash-dotted line marks the position where $\Theta = 0°$.

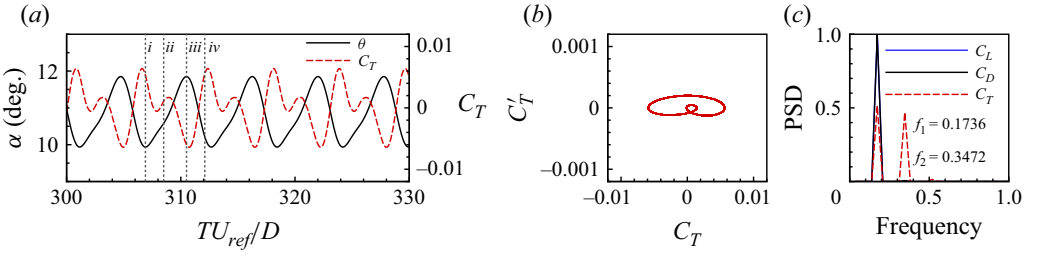


Figure 6. Kinematic characteristics of the freely falling circular cylinder with a splitter plate showing the SVOF mode ($Ga = 150$, $\rho^* = 1.01$, $L^* = 1.0$). (*a*) Time histories of α and C_T. Four instants in a motion period are labelled by the lines *i*–*iv*. (*b*) The Lissajous figure C_T–C_T'. (*c*) The PSD of C_L, C_D and C_T.

motion cycle. This is reflected in the presence of two closed cycles of different sizes on the Lissajous figure. And it leads to the appearance of the second frequency $f_2 = 0.3472$ on the power spectral density (PSD) figure (the first frequency $f_1 = 0.1736$ represents the frequency of motion).

The second frequency is attributed to the vortex shedding at distinct positions of the circular cylinder with a splitter plate. As shown in figure 7(*bi*–*biv*), flow separation is observed on one side of the circular cylinder, from which a vortex is formed. The flow on the other side first detaches from the circular cylinder, then reattaches to the splitter plate; it is coiled along the plate, and finally forms a vortex behind the splitter plate. The reattachment phenomenon has been documented in the experiments conducted by Gu *et al.* (2012). This type of wake that sheds two vortices within a single motion cycle is known as the 2S wake pattern. The pressure distribution corresponding to the vorticity contour is

https://doi.org/10.1017/jfm.2025.10590 Published online by Cambridge University Press

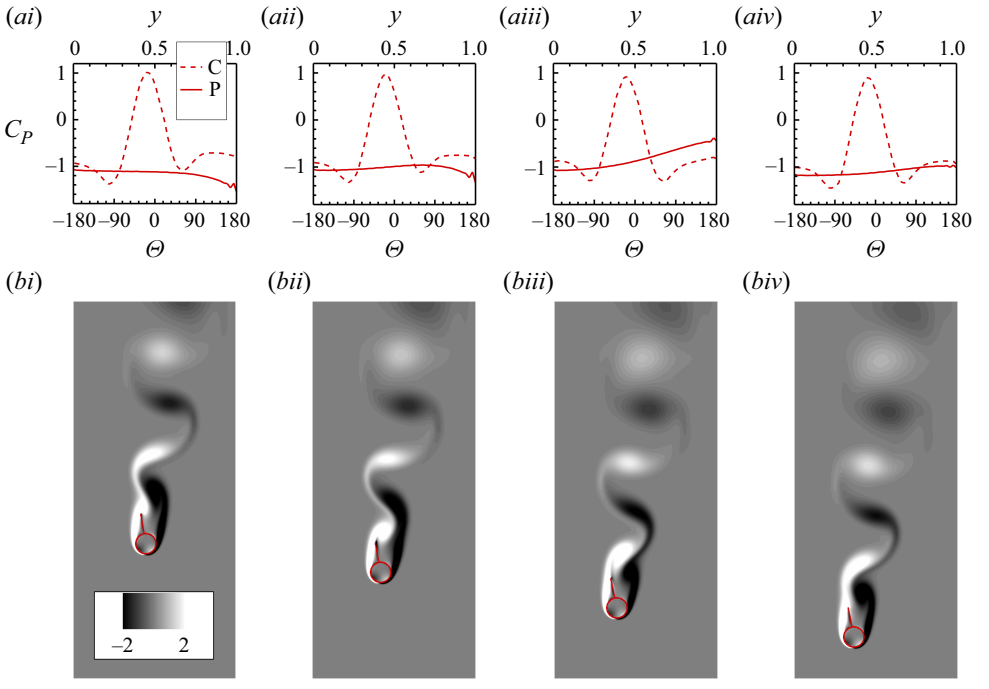


Figure 7. Vorticity contours (*b*) and the corresponding pressure distributions on the structure (*a*) for the typical case exhibiting the SVOF mode of kinematics ($Ga = 150$, $\rho^* = 1.01$, $L^* = 1.0$). Images *i–iv* illustrate the four instants in figure 6(*a*).

displayed in figure 7(*ai–aiv*). It can been seen that the stagnation point is at approximately $\Theta = -19°$. The low pressure regions are found from the side of the circular to its rear, where the pressure is significantly lower on the side to which the circular cylinder is turned, which accounts for the drift motion of the circular cylinder.

3.1.3. *The ZOF mode*

As outlined at the start of § 3.1, the amplitude of the transverse oscillation of the cases belonging to the ZOF kinematic mode is significantly larger than that of those categorised into the SVOF kinematic mode. To shed light on the transition mechanism, we plot the kinematic characteristics of the typical case ($Ga = 300$, $\rho^* = 1.20$, $L^* = 1.0$) which just enters the ZOF mode in figure 8(*a–c*). It is shown that the fluctuation of the turn angle α increases considerably, and C_T fluctuates four times in one motion cycle. The corresponding Lissajous figure C_T–C_T' contains four cycles. And the PSD of C_T presents a frequency $f_3 = 0.3572$ that is four times the frequency of motion $f_1 = 0.0893$.

Further increasing the value of Ga, clear disordered motions of the circular cylinder appear. Figure 8(*d–f*) illustrate the case at $Ga = 400$, which exhibits the worst periodicity for α and C_T in the ZOF regime. Such disorder is confirmed in the Lissajous plot. Figure 8(*f*) exhibits a dominant frequency $f_1 = 0.0859$ and some insignificant sub-frequencies, indicating that the disorder exists within each cycle of the motion.

Snapshots of the vorticity contours and the pressure distributions of the two typical cases are presented in figures 9 and 10, which illustrate the development of the disorder in the flow field. The case with relatively lower Ga exhibits the 2P wake pattern where two pairs of vortices are shed successively in one cycle of motion (see figure 9). The other case, with relatively larger Ga, presents certain disorders in the two cycles illustrated in

https://doi.org/10.1017/jfm.2025.10590 Published online by Cambridge University Press

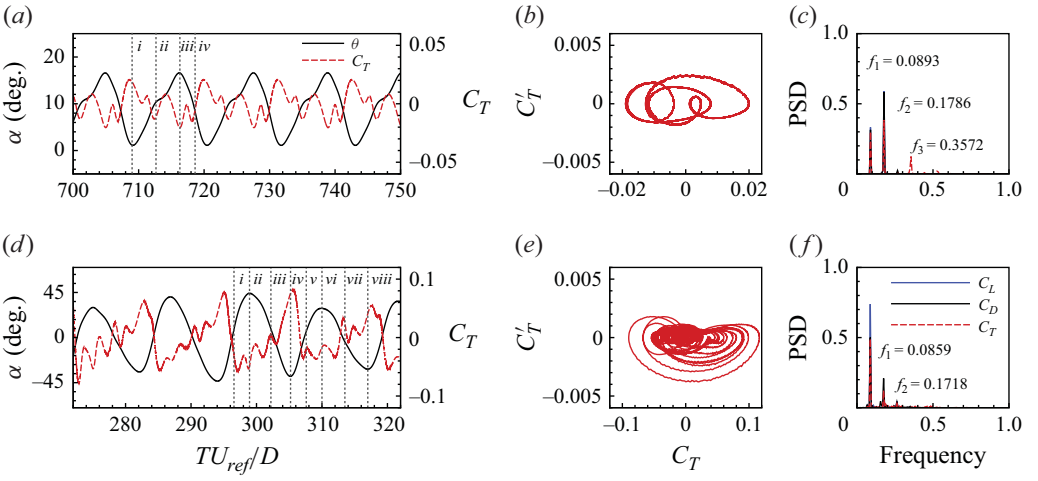


Figure 8. Kinematic characteristics of the freely falling circular cylinder with a splitter plate showing the ZOF mode of kinematics, for (*a–c*) $Ga = 300$, $\rho^* = 1.20$, $L^* = 1.0$ and (*d–f*) $Ga = 400$, $\rho^* = 1.01$, $L^* = 1.0$. (*a*,*d*) Time histories of α and C_T. (*b*,*e*) The Lissajous figure C_L–C_L'. (*c*,*f*) The PSD of C_L, C_D and C_T.

figure 10: two vortex pairs and one single vortex are shed in the first cycle of motion (see figure 10(*bi–biv*)), which forms the 2P + 1S wake pattern; and two vortex pairs and two single vortices are shed in the next cycle of motion (see figure 10(*bv–bviii*)), which belongs to the 2P + 2S wake pattern. The variations in the wake pattern exert a direct influence on the pressure distribution on the structural surface (see figure 10(*ai–aviii*)), and finally lead to subtle differences in each motion cycle. For the cases belonging the ZOF mode, this kind of disorder develops progressively as Ga increases, leading to uncertain wake patterns in each cycle of motion, which is termed the 2P + nS wake pattern in this paper.

3.1.4. *The LF mode*

As discussed at the start of § 3.1, for cases exhibiting the LF mode of kinematics, the falling trajectory of the circular cylinder with a splitter plate could finally return to the vertical path with minor transverse oscillations. Taking the case with $Ga = 800$, $\rho^* = 1.01$ and $L^* = 1.0$ as an example, the circular cylinder presents the oblique falling tendency in the initial stage, then abruptly switches to the vertical falling trajectory (see the purple line in figure 4*g*). In figure 4(*e*), it can be seen that before $TU_{ref}/D = 49$, the curves of the velocity components U_C and V_C and the angular velocity ω_C of the circular cylinder present large amplitudes of oscillation with approximately the same frequency, which is analogous to the observations in the ZOF mode. After $TU_{ref}/D = 49$, the oscillation amplitude of the vertical velocity component V_C is largely reduced, with its frequency doubled. Correspondingly, the falling trajectory of the circular cylinder is shifted to a vertical path with minor transverse oscillations. Similar mode-switching phenomena were identified in experiments of freely falling/rising spheres (Jenny *et al.* 2004). Recently, Choi *et al.* (2025) also experimentally reported a similar large-amplitude, periodic vertical motion for a freely falling sphere with a rigid rear filament at Reynolds numbers of $O(10^3)$.

Figure 11 illustrates the kinematic characteristics in the vertical falling state of the typical LF mode with $Ga = 800$, $\rho^* = 1.01$ and $L^* = 1.0$. Comparing with the earlier case with $Ga = 400$, showing the ZOF kinematic mode (see figure 8(*d–f*)), the larger Ga in this case surprisingly helps to restore the periodicity of α and C_T. Referring to the

https://doi.org/10.1017/jfm.2025.10590 Published online by Cambridge University Press

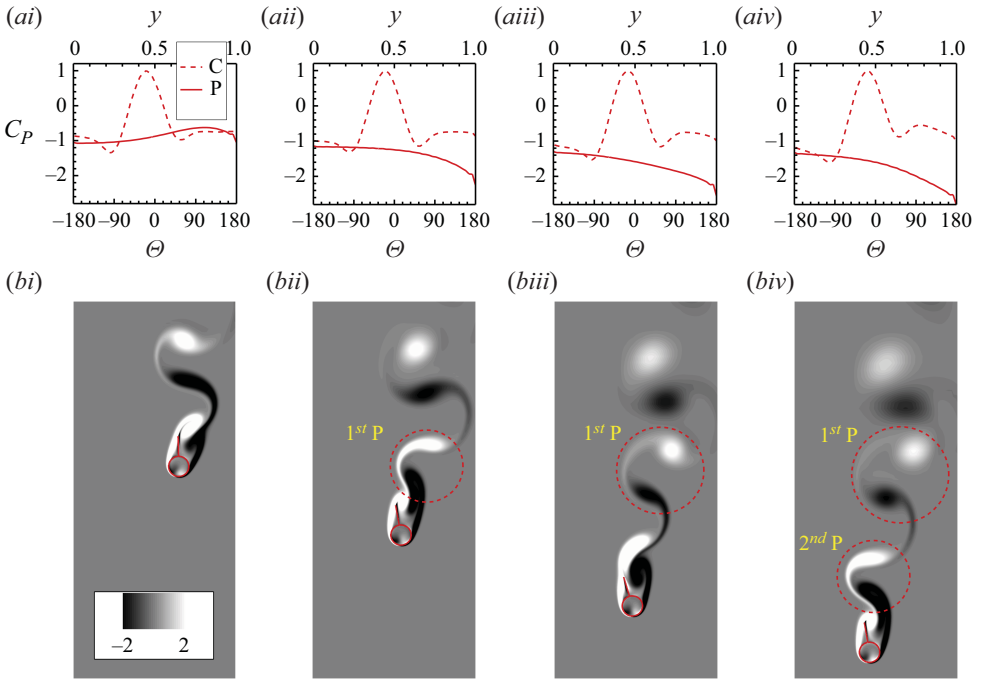


Figure 9. Vorticity contours (*b*) and the corresponding pressure distributions on the structure (*a*) for the typical case exhibiting the ZOF mode of kinematics ($Ga = 300$, $\rho^* = 1.20$, $L^* = 1.0$). Images *i–iv* illustrate the four instants in figure 8(*a*).

Lissajous figure of C_T–C_T', a concentrated centre-symmetric and polycyclic shape shows up, which suggests good periodicity and symmetry of the falling motion. Furthermore, the frequency of C_D is twice the frequency of motion $f_1 = 0.1231$ (see figure 11*c*), which is significantly different from the results for the other kinematic modes. This indicates that C_D undergoes two rounds of acceleration/deceleration in a circle of motion of the circular cylinder, whereas C_L and C_T undergo one circle. This phenomenon can be attributed to the unique wake pattern of the LF kinematic mode. As Ga increases, the fluid viscosity is weakened, which facilitates the vortex shedding. The wake of the cases belonging to the LF mode of kinematics generally follows the 2P + 2S pattern, which is also more regularised compared to the wake patterns associated with the ZOF kinematic mode. As highlighted in the red dashed circles in figure 12(*bi–biv*), the first 1P + 1S vortices are shed when the circular cylinder travels from left to right, and the subsequent 1P + 1S vortices are shed when it moves from right to left. The detachment of every set of 1P + 1S vortices would trigger fluctuations in the pressure distributions on the circular cylinder (from figure 12(*aii*) to figure 12(*aiii*), and from figure 12(*aiv*) to figure 12(*ai*)), which results in C_D being influenced twice in one cycle of motion.

3.1.5. *The CF mode*

At even higher Ga, the motion behaviour of the free fall of the circular cylinder with a splitter plate returns to a disordered manner. In this case, the kinematics may consist of multiple modes that are difficult to distinguish. For example, the grey background region in figure 4(*f*) presents short-term kinematics that is analogous to the LF mode, while the falling direction may be switched between these intermittent periods of motion. In this

https://doi.org/10.1017/jfm.2025.10590 Published online by Cambridge University Press

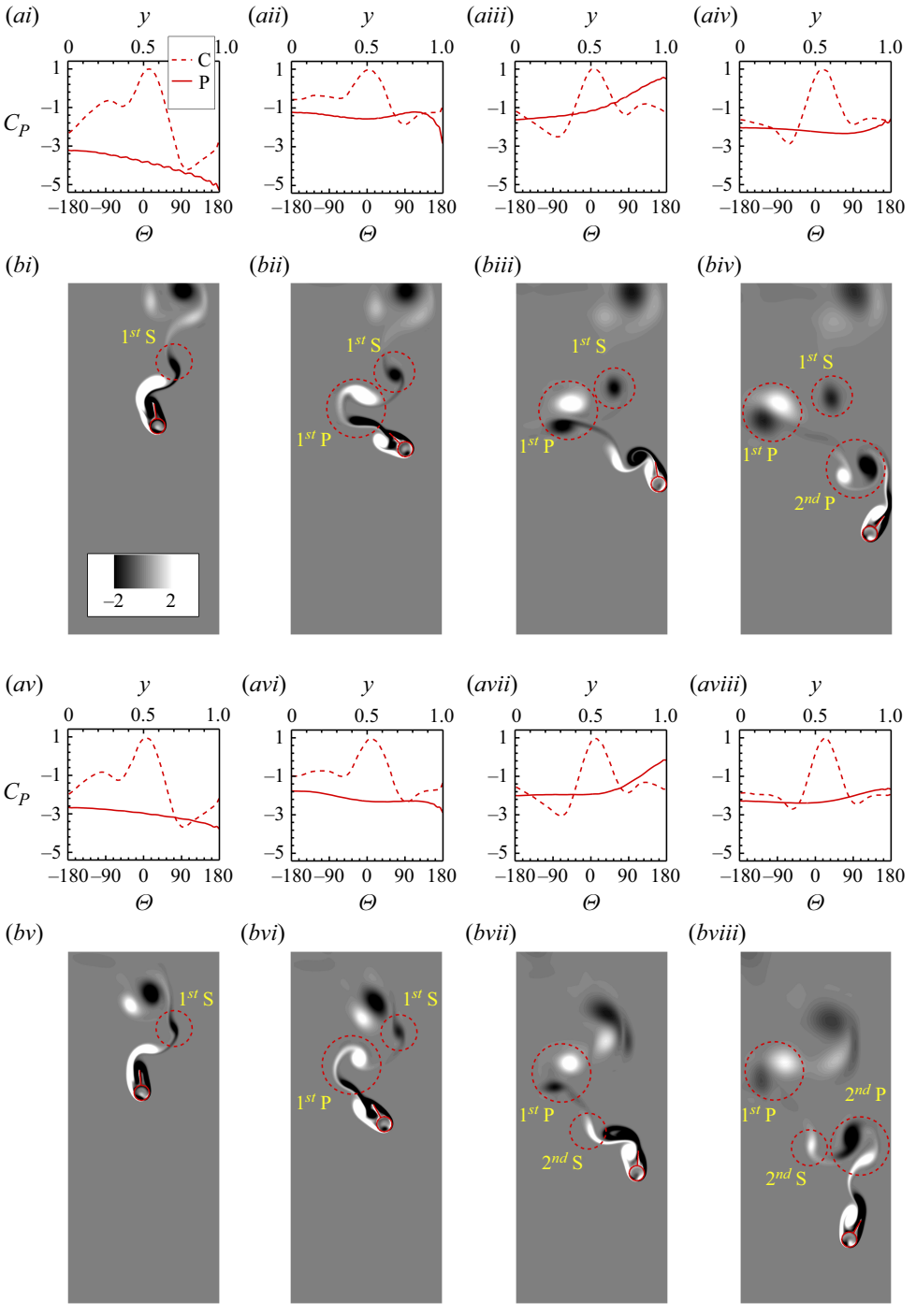


Figure 10. Vorticity contours (*b*) and the corresponding pressure distributions on the structure (*a*) for the typical case exhibiting the ZOF mode of kinematics ($Ga = 400$, $\rho^* = 1.01$, $L^* = 1.0$). Images *i–viii* illustrate the eight instants in figure 8(*d*).

https://doi.org/10.1017/jfm.2025.10590 Published online by Cambridge University Press

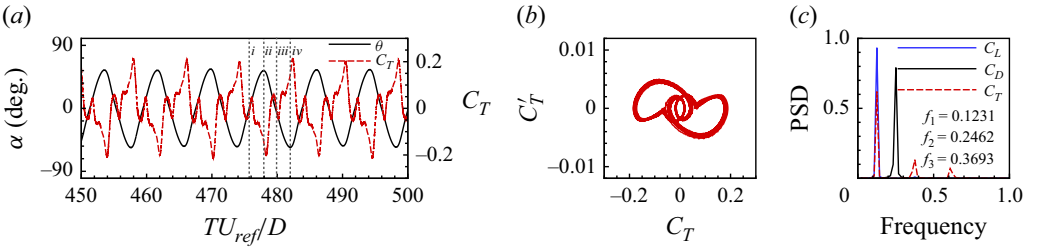


Figure 11. Kinematic characteristics of the freely falling circular cylinder with a splitter plate showing the LF mode of kinematics ($Ga = 800$, $\rho^* = 1.01$, $L^* = 1.0$). (*a*) Time histories of α and C_T. Four instants in a motion period are labelled by the lines *i*–*iv*. (*b*) The Lissajous figure C_T–C'_T. (*c*) The PSD of C_L, C_D and C_T.

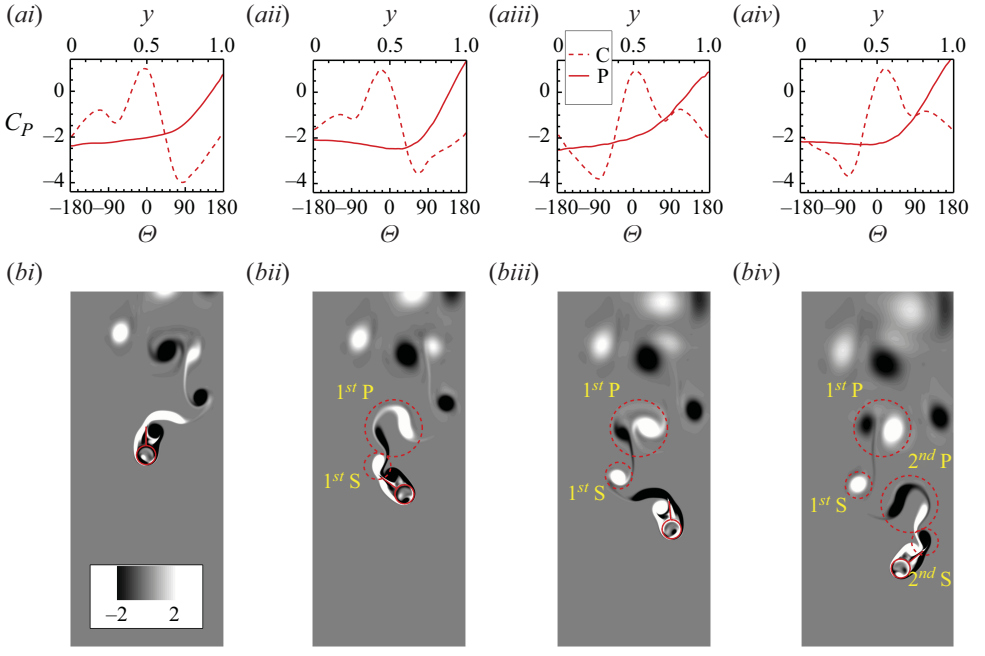


Figure 12. Vorticity contours (*b*) and the corresponding pressure distributions on the structure (*a*) for the typical case exhibiting the LF mode of kinematics ($Ga = 800$, $\rho^* = 1.01$, $L^* = 1.0$). Images *i*–*iv* illustrate the four instants in figure 11(*a*).

paper, the term 'chaotic falling' (CF) is employed to describe this particular type of falling motion.

The kinematic characteristics displayed in figure 13 reveal the pronounced chaotic behaviour of the CF mode. The time histories of α and C_T exhibit poor periodicity (see figure 13*a*), and the Lissajous map evolves to fractal distributions (see figure 13*b*), which is more intricate than the ZOF mode illustrated in figure 8(*e*), and thus indicates stronger disorders. Furthermore, the PSD diagrams of C_L, C_D and C_T present a complex broadband spectrum, and the dominance of the main frequency f_1 is no longer significant.

In order to illustrate the chaotic features of the wake pattern, four instantaneous vorticity contours in one motion cycle are shown in figure 14. Categorisation of the complex vortex structures observed in this figure to a specific wake pattern is difficult. Therefore, the term 'chaotic wake pattern' is used in this paper.

https://doi.org/10.1017/jfm.2025.10590 Published online by Cambridge University Press

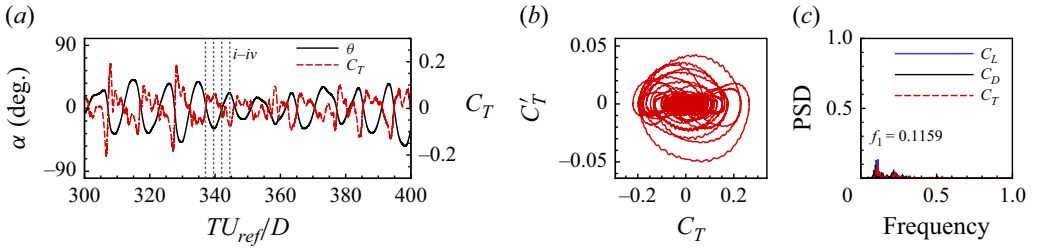


Figure 13. Kinematic characteristics of the freely falling circular cylinder with a splitter plate showing the CF mode of kinematics ($Ga = 800$, $\rho^* = 1.20$, $L^* = 1.0$). (*a*) Time histories of α and C_T. Four instants in a motion period are labelled by the lines *i–iv*. (*b*) The Lissajous figure C_T–C_T'. (*c*) The PSD of C_L, C_D and C_T.

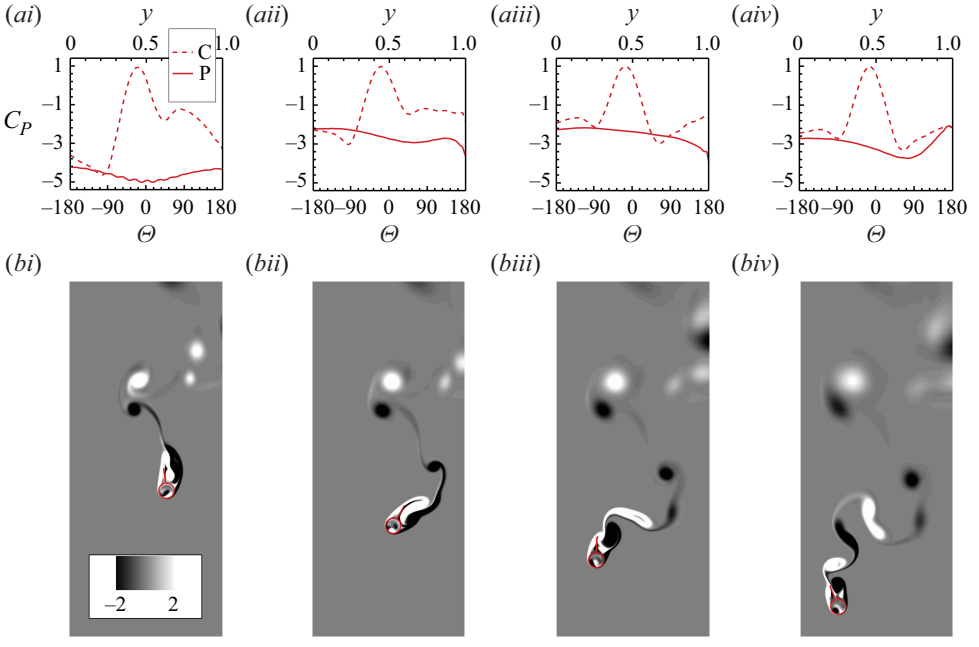


Figure 14. Vorticity contours (*b*) and the corresponding pressure distributions on the structure (*a*) for the typical case exhibiting the LF mode of kinematics ($Ga = 800$, $\rho^* = 1.20$, $L^* = 1.0$). Images *i–iv* illustrate the four instants in figure 13(*a*).

3.2. *Parametric associations of the kinematic mode and the wake pattern*

Although quantitative recognitions have been gained in Choi, Jeon & Kim (2008) that the attachment of a splitter plate behind a bluff body could suppress the vortex shedding and reduce drag and lift fluctuations, the parametric range for which the splitter plate can stabilise the freely falling motion of a circular cylinder remains unclear. To address this issue, this subsection investigates a range of cases with various plate lengths ($0.5 \leqslant L^* \leqslant 2.0$), density ratios ($1.01 \leqslant \rho^* \leqslant 2.60$) and Galileo numbers ($25 \leqslant Ga \leqslant 800$). The range of the density ratio considered here covers the real conditions of common fishes and corals.

The kinematic modes and the wake patterns of four data sets classified by the length of the splitter plate are illustrated in the phase diagram in figure 15. Each symbol represents a

https://doi.org/10.1017/jfm.2025.10590 Published online by Cambridge University Press

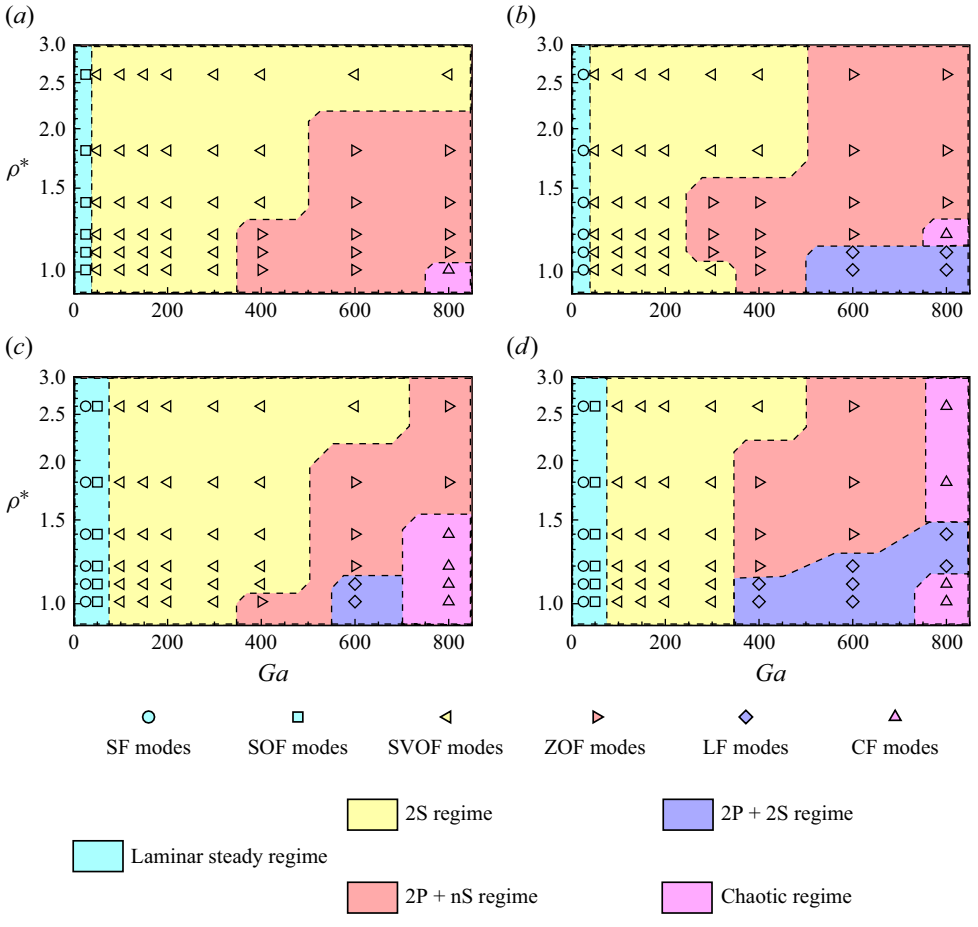


Figure 15. Overview of the typical kinematic modes and regimes of wake patterns on the $Ga-\rho^*$ diagram for the freely falling circular cylinder with a splitter plate with different lengths: (*a*) $L^* = 0.5$, (*b*) $L^* = 1.0$, (*c*) $L^* = 1.5$ and (*d*) $L^* = 2.0$. The phase diagrams are subdivided approximately into sub-regimes based on the wake patterns.

simulation case, and the background colour represents the approximate distribution regime of the wake patterns.

It is evident that cases exhibiting the SF or SOF modes of kinematics are observed in the low-Ga region. As Ga increases, the SVOF, ZOF, LF and CF modes of kinematics emerge in sequence for the freely falling circular cylinder with a splitter plate (see figure 15). To assess the mass of the splitter plate, simulations with finite plate masses ($m_p = 0.01\rho_s L$, $0.001\rho_s L$, where $\rho_s = 1.10$ g cm^{-3} and $L = 1.0$ cm) and thus modified centre of mass and moment of inertia are carried out. Figure 16 demonstrates that the kinematic modes generally remain consistent, although minor shifts of the results can be observed in the ZOF modes. This confirms that the finite mass of the splitter plate has limited influence on the freely falling motion.

Moreover, an inter-correlation between the wake pattern and the kinematic mode could be identified. The steady wake patterns are only observed at low Ga, which are insufficient for vortex shedding and thus correspond to the SF or SOF mode of kinematics. At higher Ga, the 2S wake pattern is usually associated with the SVOF mode of kinematics, while the ZOF mode of kinematics is usually correlated with the 2P + nS

https://doi.org/10.1017/jfm.2025.10590 Published online by Cambridge University Press

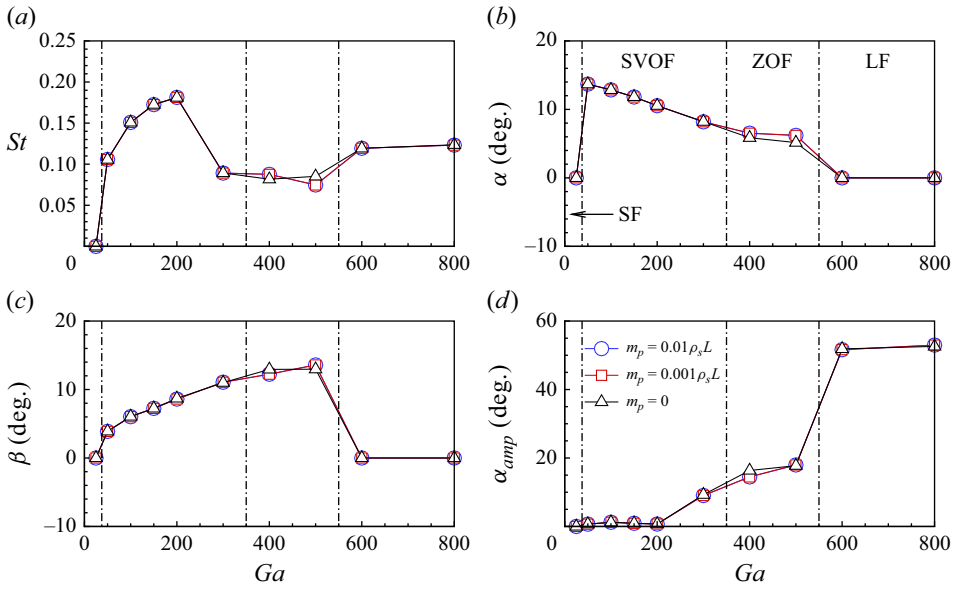


Figure 16. Numerical results of the Strouhal number St, the turn angle α, the drift angle β, and the amplitude of the turn angle α_{amp} obtained by set-ups with different plate mass.

wake pattern. A thorough examination of the available data reveals that the 2P + 2S wake pattern is observed in the wake of cases exhibiting the LF mode of kinematics. In such circumstances, the motion and the wake pattern of the circular cylinder are interconnected, resulting in enhanced periodicity. However, as Ga is increased further, the lock-in between the cylinder motion and the wake pattern is disrupted, and the chaotic features emerge in both the cylinder motion and its ambient flow pattern. Consequently, the wakes of the cases belonging to CF mode of kinematics are classified into the chaotic wake pattern. In addition, evidence suggests that the LF modes are more likely to occur at lower ρ^*. This phenomenon can be explained by the principle that structures with low ρ^* have smaller inertia and thus are more susceptible to the hydrodynamic forces, which can result in the LF modes. In contrast, structures with high ρ^* possess larger inertia, leading to a delay in the transition of the kinematic mode and the wake pattern with the growth of Ga.

3.3. *The oscillation amplitude of the turn angle*

A noteworthy discovery from § 3.1 is the significant variation in the oscillation amplitude of the turn angle of the circular in different cases. Figure 17 shows the phase diagram of the oscillation amplitude of the turn angle α_{amp}. It is evident that α_{amp} increases gradually with Ga, and is related to the kinematic modes. The magnitude of α_{amp} for each kinematic mode is found to be LF > CF > ZOF > SVOF > SOF = SF = 0, where a steep gradient exists at the boundary between the SVOF mode and the ZOF/LF modes. This transition can be considered as a shift between the gravity-dominated modes (SF/SOF/SVOF) and the hydrodynamic-dominated modes (ZOF/LF/CF). The former represents that the falling motion of the structure is dominated by steady gravity, which is characterised by small oscillation amplitude of its self-rotation that presents minor variation with increasing Ga at the same ρ^*. The latter represents motions dominated by the hydrodynamic forces, as evidenced by the surging oscillation amplitudes of self-rotation with increasing Ga at the same ρ^*. Furthermore, it is notable that the gravity-dominated modes with higher ρ^* could

https://doi.org/10.1017/jfm.2025.10590 Published online by Cambridge University Press

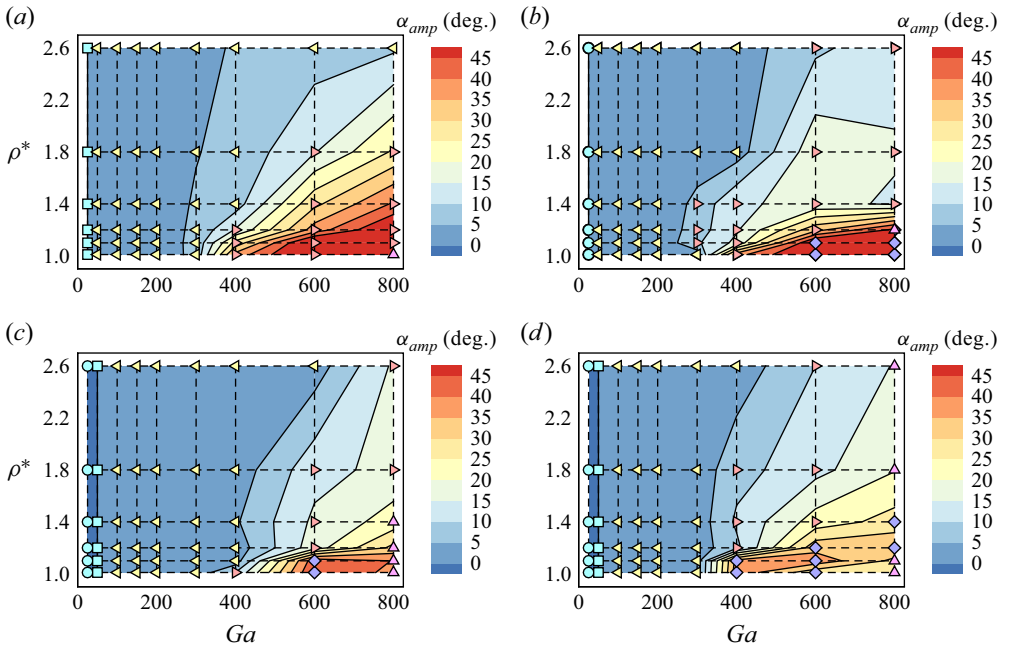


Figure 17. Diagrams of the oscillation amplitude of the turn angle α_{amp} on the phase space of Ga and ρ^*. The images present the phase diagrams at different lengths L^* of the splitter plate: (*a*) $L^* = 0.5$, (*b*) $L^* = 1.0$, (*c*) $L^* = 1.5$ and (*d*) $L^* = 2.0$. The symbols are filled with distinct colours as assigned in figure 15 for the specific wake pattern.

emerge at higher Ga, which is analogous to the study of Seyed-Ahmadi & Wachs (2019) on the velocity fluctuations of spheres.

3.4. *The falling velocity*

As stated in § 3.1, the attachment of the splitter plate to the rear of the circular cylinder can tilt its falling trajectory. In such cases, the falling velocity would have the horizontal and vertical components. In this subsection, the phase diagrams of the two velocity components are presented to investigate their contributions in the falling motion. Specifically, to illustrate the significance of the horizontal velocity component U in the total falling velocity U_{ref}, the normalised horizontal velocity U/U_{ref} is used in figure 18. Meanwhile, to shed light on the effect of the splitter plate, the vertical velocity component V is normalised by the falling velocity of the freely falling bare circular cylinder with the same parametric settings ($U_{ref(L^*=0.0)}$), as shown in figure 19.

As shown in figure 18, it is evident that as Ga increases, the contributions from the horizontal component of the falling velocity grow until the onset of the ZOF mode. Thereafter, the normalised horizontal velocity decreases, and finally approaches zero after entering the regimes of the LF or CF modes. Furthermore, it is found that specific L^* and ρ^* enable the circular cylinder to possess larger horizontal velocities. For example, the case $L^* = 1.5$, $\rho^* = 1.8$ at $Ga = 600$ has the largest normalised horizontal velocity among all cases.

It is interesting that in most cases, attaching the splitter plate to the rear of the circular cylinder would accelerate its falling. In the cases with low Ga or large ρ^* that exhibit oblique falling mode, the vertical velocity component is larger than that of the bare circular cylinder (note that the horizontal velocity component of the bare circular cylinder in these

https://doi.org/10.1017/jfm.2025.10590 Published online by Cambridge University Press

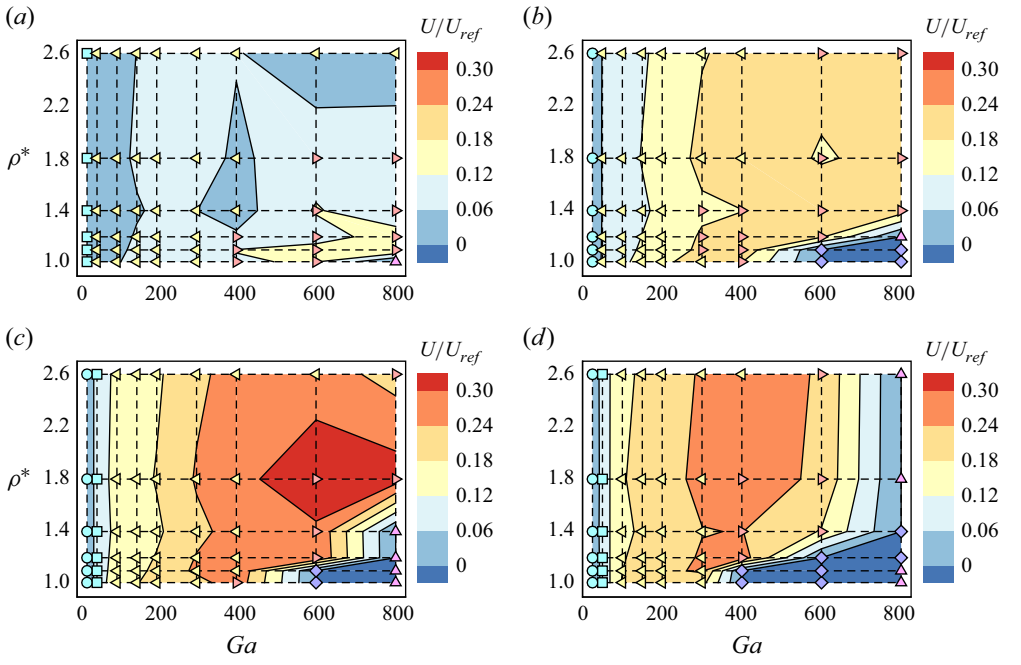


Figure 18. Diagrams of the normalised horizontal velocity U/U_{ref} on the phase space of Ga and ρ^*. The images present the phase diagrams at different lengths L^* of the splitter plate: (*a*) $L^* = 0.5$, (*b*) $L^* = 1.0$, (*c*) $L^* = 1.5$ and (*d*) $L^* = 2.0$. The symbols are filled with distinct colours assigned as in figure 15 for the specific wake pattern.

cases is negligible, therefore $U_{ref\,(L^*=0.0)}$ can represent its vertical velocity component). Furthermore, the acceleration induced by the presence of the splitter plate is more pronounced at higher Ga. However, for cases belonging to the LF mode of kinematics, a deceleration effect could emerge in the presence of the splitter plate. This is consistent with recent experiments (Choi *et al.* 2025) on a freely falling sphere with a filament, which exhibit a large-amplitude zigzag motion with a deceleration in the vertical velocity. This deceleration can be attributed to the distinct locations of vortex shedding. For the cases belonging to the LF mode, the vortex shedding occurs closely behind the circular cylinder (see figure 12*b*), which results in the low pressure region in its downstream vicinity and thus provides resistance to the falling. And the vertical velocity component V undergoes two rounds of acceleration/deceleration within one cycle of motion, as discussed in § 3.1.4. For the cases of the SVOF and ZOF modes, vortex shedding occurs on the downstream slanting side of the structure, due to which the low pressure region is relatively more distant from the cylinder surface, and the suction effect is reduced. In these cases, the vertical velocity component V normally experiences one acceleration/deceleration process within one cycle of motion.

Moreover, it is found that in the gravity-dominated modes (SF/SOF/SVOF), the phase diagrams of the horizontal and vertical velocity components show a predominantly vertical distribution, while in hydrodynamic-dominated modes (ZOF/LF/CF), the phase diagrams of the two velocity components both show a predominantly horizontal distribution. This observation indicates that in the gravity-dominated modes, the horizontal and vertical velocity components are less influenced by the density ratio ρ^*, suggesting a strong correlation between Ga and the falling velocity in these instances. Conversely, in hydrodynamic-dominated modes, velocity fluctuations resulting from vortex shedding

https://doi.org/10.1017/jfm.2025.10590 Published online by Cambridge University Press

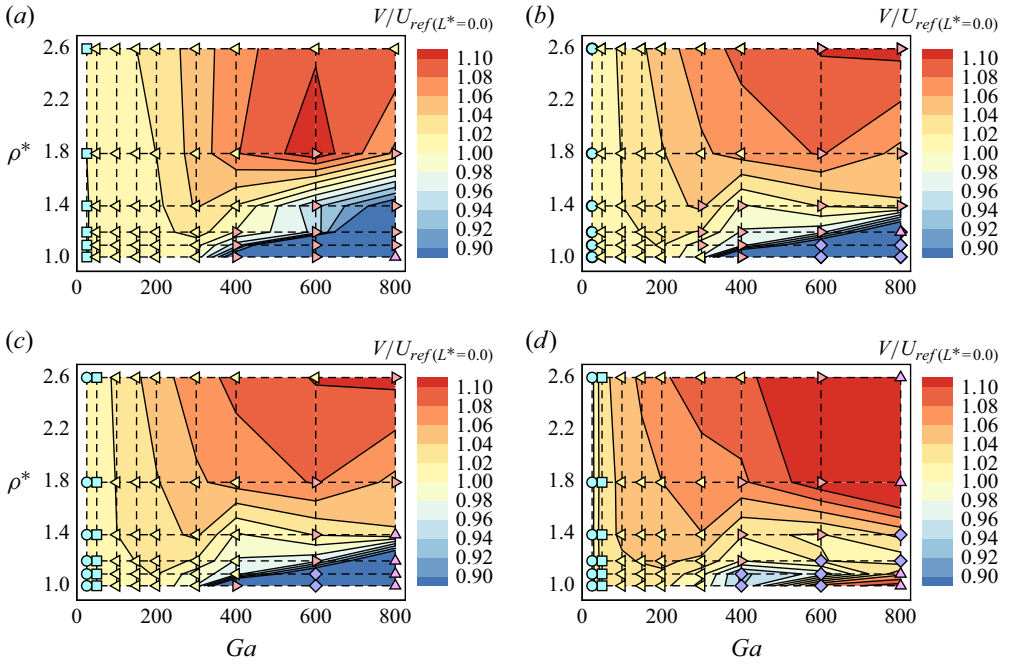


Figure 19. Diagrams of the normalised vertical velocity $V/U_{ref(L^*=0.0)}$ on the phase space of Ga and ρ^*, where $U_{ref(L^*=0.0)}$ is the reference velocity of the freely falling bare circular cylinder with the same Ga and ρ^*. The images present the phase diagrams at different lengths L^* of the splitter plate: (*a*) $L^* = 0.5$, (*b*) $L^* = 1.0$, (*c*) $L^* = 1.5$ and (*d*) $L^* = 2.0$. The symbols are filled with distinct colours as assigned in figure 15 for the specific wake pattern.

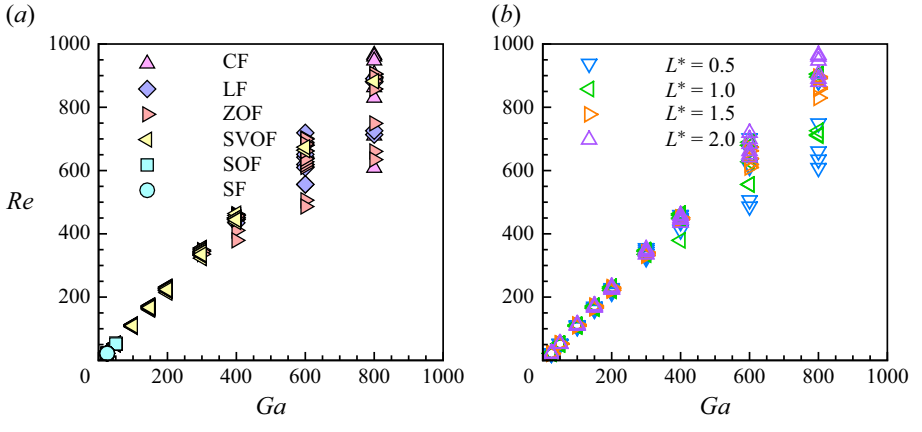


Figure 20. (*a*) The Reynolds number Re for different kinematic modes as a function of the Galileo number Ga. (*b*) The Reynolds number Re for different splitter plate lengths as a function of the Galileo number Ga.

substantially modulate the kinematics, resulting in the decoupling between Ga and the falling velocity.

Figure 20 reveals the relationship between the Reynolds number and the Galileo number in different kinematic modes and for different lengths of the splitter plate. For the gravity-dominated modes, the reference velocity is determined by the balance between the gravity and the relatively steady drag force. And Re demonstrates a quasi-linear correlation with

https://doi.org/10.1017/jfm.2025.10590 Published online by Cambridge University Press

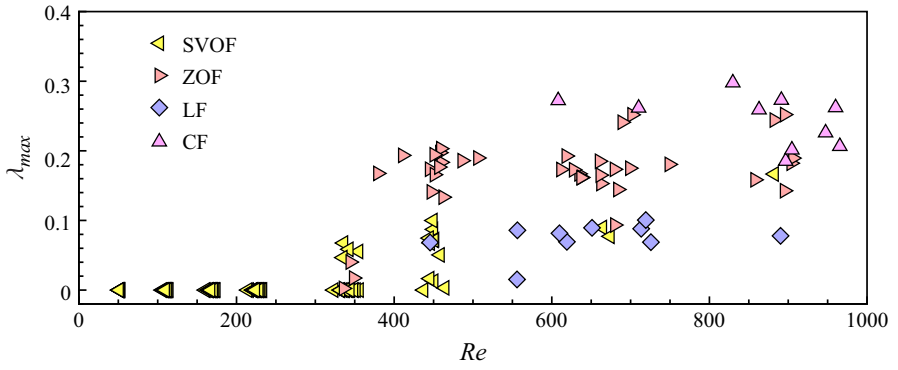


Figure 21. The variation of the maximum Lyapunov exponents λ_{max} with Re for the rotational component of the freely falling motion of the circular cylinder with a splitter plate.

Ga. In contrast, the hydrodynamic-dominated modes show significant deviations from this trend, which are characterised by large, unsteady oscillations driven by the complex vortex shedding behaviours. In this regime, the splitter plate becomes a crucial participant when it contributes to the unsteady dynamics, which substantially modulates the falling velocity.

3.5. *Lyapunov exponent analysis for kinematics*

While § 3.1 illustrated the chaotic features of the system via PSD and phase-space Lissajous figures, a more quantitative measure can be obtained through the computation of the maximum Lyapunov exponent λ_{max} (see A.3 for the explanation of λ_{max}). As shown in figure 21, the data are categorised into four distinct kinematic modes, each represented by different symbols. It is evident that the chaotic behaviours in the system grow with Re. The maximum Lyapunov exponents are all negligible at low Reynolds numbers, indicating that the motions of the SVOF modes in this range exhibit periodic behaviours. At higher Reynolds numbers, other kinematic modes show up, which is accompanied by a significant increase in λ_{max}, implying the growth of flow complexity and the emergence of non-periodic behaviours. In particular, the LF modes have smaller values of λ_{max}, while the CF modes have higher values of λ_{max}, exceeding 0.2 at many points. This divergence in trends reveals different mechanisms: the LF modes have more ordered motions at higher values of Re, while the CF modes develop more chaotic motions.

3.6. *Estimation of the Strouhal number*

In this subsection, further investigation of the vortex shedding frequency, which is characterised by the Strouhal number, is carried out. For the present study of a freely falling circular cylinder with a splitter plate, given the complexity and disorder of vortex shedding at larger Re, the analysis of the Strouhal number conducted here is limited to the Reynolds number that makes the maximum Lyapunov exponent negligible.

The analysis starts from the established relationship between the vortex shedding frequency St and the Reynolds number Re for the vortex shedding frequency of flow past a fixed circular cylinder (Williamson & Brown 1998), which reads

$$St_{fixed} = k_A + \frac{k_B}{\sqrt{Re}}, \tag{3.1}$$

https://doi.org/10.1017/jfm.2025.10590 Published online by Cambridge University Press

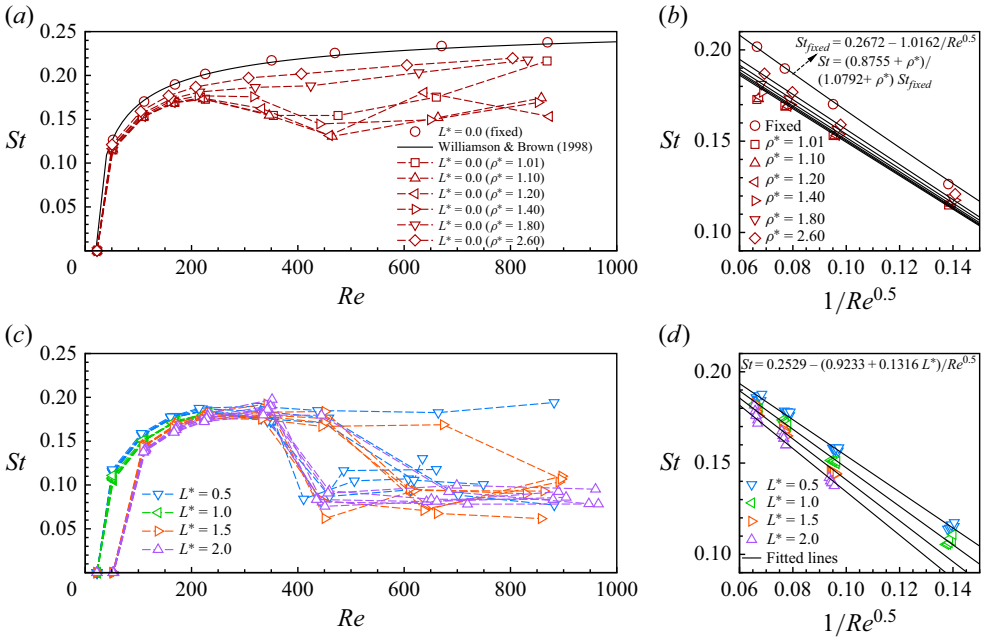


Figure 22. (*a*) The relationship between Re and St for a freely falling bare circular cylinder and a fixed circular cylinder, compared with the results in Williamson & Brown (1998). The dashed lines include case series with six different density ratios, i.e. $\rho^* = 1.01$, 1.10, 1.20, 1.40, 1.80 and 2.60. (*b*) The $Re^{-0.5}-St$ relation for a freely falling bare circular cylinder. The symbols are the results of the present study, and the solid lines are the fitted results given by Namkoong *et al.* (2008). (*c*) The relationship between Re and St for a freely falling circular cylinder with different lengths of splitter plate and six different density ratios. (*d*) The $Re^{-0.5}-St$ relation for a freely falling circular cylinder with different lengths of splitter plate and six different density ratios.

where k_A and k_B are two constants. Here, k_A is related to the geometry of the structure, and $k_B/\sqrt{Re}$ is related to the thickness of the shear layer (Williamson & Brown 1998). Figure 22(*a*) shows the good agreement between the present results and the reference data of Williamson & Brown (1998) ($k_A = 0.2665$ and $k_B = -1.0180$). Also included in this figure are the results of six different density ratios. A general tendency is that St would grow as Re increases. At the same Re, the variation of the density ratio affects the value of St. The relation between St and Re for the freely falling circular cylinder with different density ratios can be established based on the linear correlation between St and ρ^* as proposed by Namkoong *et al.* (2008):

$$St = \left(\frac{\rho^* + k_C}{\rho^* + k_D}\right) St_{fixed} = \left(\frac{\rho^* + k_C}{\rho^* + k_D}\right)\left(k_A - \frac{k_B}{\sqrt{Re}}\right), \tag{3.2}$$

where k_C and k_D are constants, and St_{fixed} is obtained from (3.1). Namkoong *et al.* (2008) reported the constants as $k_A = 0.2672$, $k_B = -1.0162$, $k_C = 0.8755$ and $k_D = 1.0792$. Figure 22(*b*) shows the comparison between the present results and those of Namkoong *et al.* (2008). Note that the leftmost set of data ($Re \cong 210$) deviates slightly from the fitted results due to the surging instability of the wake. For $Re \leqslant 190$, the prediction equation (3.2) presents appealing accuracy.

For a freely falling bare circular cylinder, the shedding frequency is strongly correlated with the inertia of the circular cylinder (ρ^*), as its oscillatory response dictates the vortex

https://doi.org/10.1017/jfm.2025.10590 Published online by Cambridge University Press

shedding process. However, the attachment of a splitter plate fundamentally alters this dynamic. The effect of the density ratio and the plate length on St is illustrated in figure 22(c), which demonstrates correlations between these parameters. The attachment of the splitter plate stabilises the near wake and delays vortex formation, causing the shedding dynamics to be governed primarily by the geometry of the combined body and the development of viscous shear layers along its surfaces. This geometric and viscous control of the wake is the dominant mechanism, which overshadows the influence of the inertia of the circular cylinder (ρ^*). However, it is observed that the length of the splitter plate could alter the vortex shedding frequency significantly. In the range $Re \leqslant 260$, and considering cases with vortex shedding (i.e. $St \neq 0$), the freely falling circular cylinder with a splitter plate exhibits the SVOF mode of kinematics, which corresponds to shedding two opposite vortices from the circular cylinder and the splitter plate within a single cycle of motion. Therefore, modification should be made to (3.1) to reflect the role of the plate length, which is tentatively proposed as

$$St = k_A + \frac{k_B + k_C \times L^*}{\sqrt{Re}}, \tag{3.3}$$

where k_A is a constant related to the geometry of the structure, and $k_B/\sqrt{Re}$ and $k_C/\sqrt{Re}$ are related to the thicknesses of the shear layers on the circular cylinder and on the plate, respectively. Fitted values of the constants are $k_A = 0.2529$, $k_B = -0.9223$ and $k_C = -0.1316$. And the fitted results show good agreement with the simulation data, as presented in figure 22(d).

3.7. *Estimation of angles*

In the range of parameters considered in this paper, attaching a splitter plate to the rear of a freely falling circular cylinder could alter its kinematic characteristics. The circular cylinder may rotate to the turn angle α, and its falling trajectory is tilted to the drift angle β (see figure 23). This subsection will discuss the estimation of these two important angles. It should be noted that the analysis in this subsection is based on the assumption of a quasi-steady state that can determine specific values of the angles, due to which unsteady cases, such as those belonging to the ZOF, LF or CF modes with significant oscillation amplitudes in their rotating angles, have been excluded from the present discussion. Figures 24(c) and 24(e) show the variation of angles α and β with the Reynolds number. It can be observed that in the range $Re > 50$ (except the cases with $L^* = 0.5$), the turn angle α is decreasing with Re, while the drift angle β undergoes a gradual increase.

The turn angle α and the drift angle β should be related to the forces acting on the structure. When the circular cylinder with a splitter plate falls in the fluid, the hydrodynamic forces and the gravity are balanced over the course of time. Figure 23 shows the time-averaged vorticity contour, the gravity G, the time-averaged hydrodynamic forces f_x and f_y on the plate, and F_x and F_y on the circular cylinder. The force balance relationship can be expressed as

$$F_x + f_x = 0, \tag{3.4}$$

$$F_y + f_y = G - \rho g V_B = (\rho_s - \rho) g V_B, \tag{3.5}$$

$$f_x l_x \cos(\alpha) + f_y l_y \sin(\alpha) + \frac{F_\tau D}{2} = 0, \tag{3.6}$$

where l_x and l_y are the average arms of f_x and f_y about the centre of the circular cylinder, respectively, V_B is the volume of the structure, and F_τ is the tangential hydrodynamic force acting on the surface of the circular cylinder. It should be noted that l_x and l_y do

https://doi.org/10.1017/jfm.2025.10590 Published online by Cambridge University Press

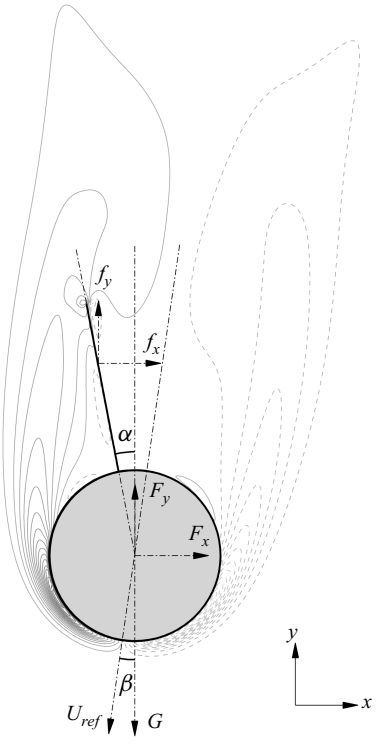


Figure 23. Time-averaged schematic with vorticity and structure contour.

not necessarily correspond to one another. Performing the first-order Taylor expansion for $\cos(\alpha)$ and $\sin(\alpha)$, and substituting (3.5) into (3.6), the estimation formulation for the turn angle α can be derived as

$$\alpha = -\frac{f_x l_x}{f_y l_y} - \frac{F_\tau D}{2 f_y l_y} \cong k_1 \frac{f_x}{(\rho_s - \rho) g V_B} L^* + A, \tag{3.7}$$

where it is assumed that $L^* \cong l_x / l_y$, $f_y = (\rho_s - \rho) g V_B - F_y \cong (\rho_s - \rho) g V_B / k_1$, k_1 is a correction factor, and A is a constant that represents the second term in (3.7) resulting from the operation.

The estimation formulation of the drift angle β can be derived as

$$\beta = \tan^{-1}\left(\frac{\mathrm{d}x}{\mathrm{d}y}\right) = \tan^{-1}\left(\frac{UT}{VT}\right) \cong \tan^{-1}\left(\frac{F_t}{F_d}\right) \cong k_2 \frac{f_x}{(\rho_s - \rho) g V_B}, \tag{3.8}$$

where $\mathrm{d}x$ and $\mathrm{d}y$ are the horizontal and vertical displacements of the structure in unit time, respectively, U and V_B are the horizontal and vertical velocities, respectively, T is the unit time, F_t and F_d are the drift and drag forces, respectively, and k_2 is a correction factor. The components F_x and f_x ensure the force balance in the horizontal direction, while the components F_y and f_y counteract $(\rho_s - \rho) g V_B$, thereby maintaining equilibrium in the vertical direction. Therefore, the variables F_t and F_d can be replaced with f_x and $(\rho_s - \rho) g V_B$, respectively.

Assuming that the force f_x on the plate is a steady force, and considering the effect of viscosity, f_x can be estimated by

$$f_x = k_3 \rho U_{ref}^2 L \sqrt{Re}, \tag{3.9}$$

https://doi.org/10.1017/jfm.2025.10590 Published online by Cambridge University Press

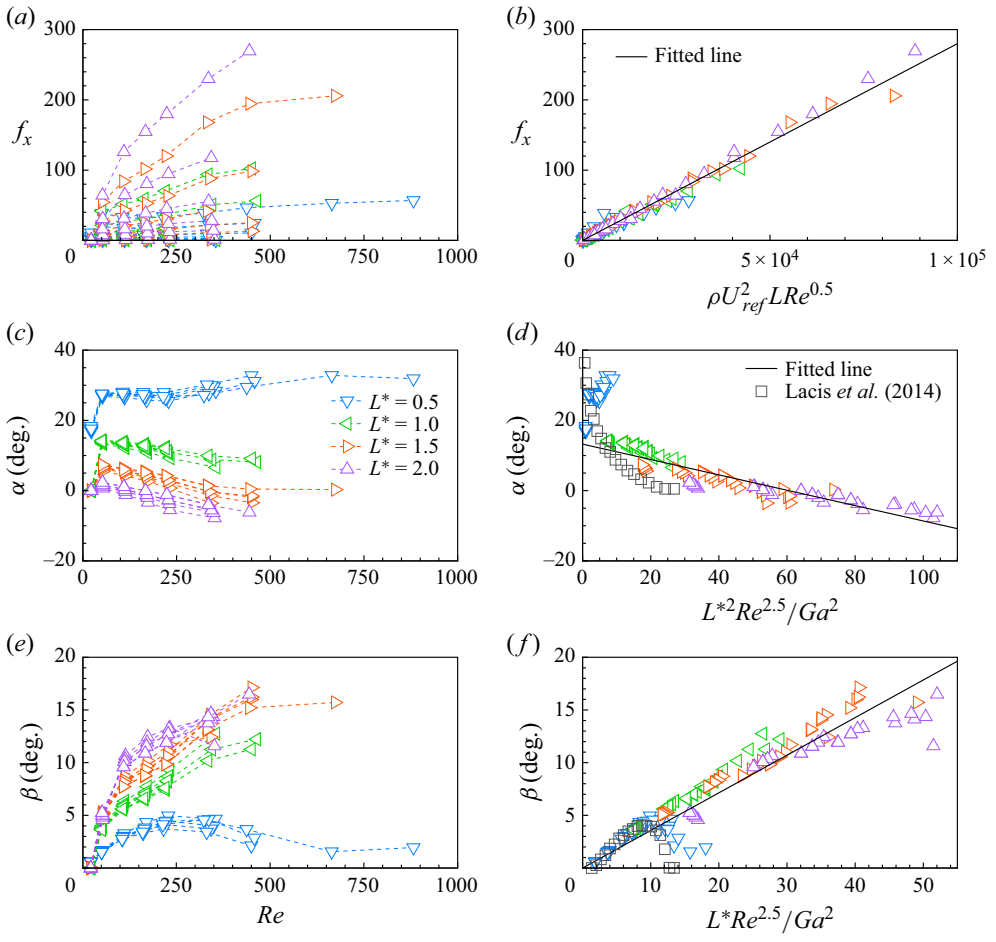


Figure 24. The variation of (*a*) the time-averaged hydrodynamic force f_x, (*c*) the turn angle α, and (*e*) the drift angle β with Re. (*b*) The force f_x as a function of $\rho U_{ref}^2 L\, Re^{0.5}$. (*d*) The turn angle α as a function of $L^{*2}\, Re^{2.5}/Ga^2$. (*f*) The drift angle β as a function of $L^*\, Re^{2.5}/Ga^2$.

where k_3 is a correction factor that accounts for the attack angle of the splitter plate and other geometric effects.

Figures 24(*a*) and 24(*b*) show the variation of f_x with Re and the fitted results based on the above estimation formulations, respectively. It can be observed that the fitting is quite satisfactory with $k_3 = 0.0028$. It should be noted that f_x is a dimensional quantity.

It is observed that (3.7) and (3.8) have the common term $f_x/(\rho_s - \rho)gV_B$, which can be simplified by substituting (3.9):

$$\frac{f_x}{(\rho_s - \rho)gV_B} = \frac{4k_3}{\pi} L^* \frac{Re^{2.5}}{Ga^2}. \tag{3.10}$$

The remaining free parameters in the estimations (3.7) and (3.8) for the turn angle α and the drift angle β can be readily obtained by fitting the present simulation results, which gives the final estimations as $\alpha \cong -0.2187 L^{*2}\, Re^{2.5}/Ga^2 + 13.2333$ and $\beta \cong 0.3569 L^*\, Re^{2.5}/Ga^2$. Figures 24(*d*) and 24(*f*) illustrate the fitted results for the present simulation and the validation of the above estimation formulations against the reference data in Lācis *et al.* (2014) ($0.2 \leqslant L^* \leqslant 2.0$). Quite good agreement with the simulation

https://doi.org/10.1017/jfm.2025.10590 Published online by Cambridge University Press

results is shown in these figures, which implies the rationale of the above analyses stemming from the force balance perspective. It should be noted that the effectiveness of the estimation formulas presented in this subsection are subject to certain limitations when being applied to a wider range of parameters. In particular, the estimation of α could deteriorate in the cases with shorter plate lengths, when the turn angle may exhibit large values, e.g. the case $L^* = 0.5$ and the first few data points in Lācis *et al.* (2014) in figure 24(*d*). The reason for such deterioration is that the first-order Taylor expansion employed in the derivation could bring a large truncation error in these circumstances. In addition, larger plate length can help to stabilise the structure and thus remove the symmetry breaking characteristic (e.g. the case with $L^* = 2.0$ and $Re = 45$ in Lācis *et al.* (2014), where the prediction of the turn angle β is no longer available). Furthermore, when the Reynolds number is high, the estimation of β may expect larger deviation. As general guideline for applications of the estimation formulas, cases with Reynolds number $Re < 260$ and the length of the splitter plate $0.5 < L^* < 2.0$ can expect good accuracy of prediction, while the estimation accuracy for cases beyond these ranges of parameters may depend on whether a quasi-steady kinematic mode can be revealed. Nevertheless, the estimations of the turn angle and the drift angle presented in this subsection shed light on the underlying mechanisms of the freely falling circular cylinder with a splitter plate, and could be of reference value to engineering applications such as inclined landing.

4. Concluding remarks

In this paper, numerical investigation of a freely falling circular cylinder attached to a splitter plate in an infinite fluid domain under gravity is carried out, using the lattice Boltzmann flux solver and the immersed boundary method. Variations of key dimensionless parameters, including the length of the splitter plate ($0.5 \leqslant L^* \leqslant 2.0$), the Galileo number ($25 \leqslant Ga \leqslant 800$) and the density ratio of the circular cylinder to the fluid ($1.01 \leqslant \rho^* \leqslant 2.60$), are considered. The following conclusions can be drawn from the results presented.

(i) The kinematics of the freely falling circular cylinder with a splitter plate can be categorised into the steady falling (SF), the steady oblique falling (SOF), the small vibration oblique falling (SVOF), the zigzag oblique falling (ZOF), the locked falling (LF) and the chaotic falling (CF) modes. The falling modes show dependency on dimensionless parameters such as the plate length, the Galileo number and the density ratio.

(ii) The wake patterns of the freely falling circular cylinder with a splitter plate are identified, and a correlation between the wake patterns and the kinematic modes is revealed. The wake pattern can be categorised into four types: the steady wake, the 2S, the 2P + nS, the 2P + 2S, and the chaotic wake, which correspond to the SF/SOF, SVOF, ZOF, LF and CF modes of kinematics, respectively.

(iii) The influence of ρ^* on the vortex shedding frequency would be diminished by attaching a splitter plate to the freely falling circular cylinder. Namkoong *et al.* (2008) found a linear relationship between vortex shedding frequency St and ρ^* for the freely falling circular cylinder without a splitter plate. However, the attachment of a splitter plate to the rear of the circular cylinder could greatly alter the Strouhal number, and enlarge the effect posed by the fluid viscosity. A correlation formulation has been established based on the vortex shedding characteristics to quantify the effect of the plate length and the Reynolds number on the Strouhal number, which shows good agreement with the numerical results.

https://doi.org/10.1017/jfm.2025.10590 Published online by Cambridge University Press

(iv) Attachment of a splitter plate can rotate the freely falling cylinder to the turn angle α and tilt its falling trajectory to the drift angle β. At a fixed value of Re, larger L^* results in smaller α and larger β. Force balance analyses have been carried out in quasi-steady conditions, which give estimation formulations for the turn angle α and the drift angle β. The estimation formulations have shown good accuracy in numerical tests, although their limitations in cases with short plate lengths or at high Reynolds numbers should be admitted.

Acknowledgements. The authors would like to thank Professor C. Shu at the National University of Singapore and Professor Y. Wang at Nanjing University of Aeronautics and Astronautics for valuable discussions and for providing the basic codes of the lattice Boltzmann flux solver. The first author would also like to thank Dr B. Zhang for insightful discussions.

Funding. This work was supported by the National Natural Science Foundation of China (grant nos 52201329 and 52471333), the Oceanic Interdisciplinary Programme of Shanghai Jiao Tong University (project number ∗SL2022PT105∗), and the Fundamental Research Funds for the Central Universities.

Declaration of interests. The authors report no conflict of interest.

Appendix A. Numerical method

A.1. *The lattice Boltzmann flux solver in arbitrary Lagragian–Eulerian coordinates*

To reduce computational efforts, the problem is resolved in a moving frame, which introduces compensation terms to the original Navier–Stokes equations. Numerical discretisation of the governing equation is then carried out by the ALE-based lattice Boltzmann flux solver (Wang *et al.* 2015, 2017), which gives

$$\frac{\partial \rho \boldsymbol{u}}{\partial t} + \nabla(\varPi - \rho \boldsymbol{u}\boldsymbol{u}_{grid}) = \boldsymbol{f}, \tag{A1}$$

$$\frac{\partial \rho}{\partial t} + \nabla\left(\sum_{\alpha=0}^{N} \boldsymbol{e}_\alpha f_\alpha^{eq} - \rho \boldsymbol{u}_{grid}\right) = 0, \tag{A2}$$

where $\boldsymbol{u}_{grid}$ is the velocity of the computational grid. The mass and the momentum fluxes are reconstructed on the cell interface with local solutions to the lattice Boltzmann equation

$$\sum_{\alpha=0}^{N} e_\alpha f_\alpha^{eq} = \rho \boldsymbol{u}, \tag{A3}$$

$$\varPi = \sum_{\alpha=0}^{N} (\boldsymbol{e}_\alpha)_\beta (\boldsymbol{e}_\alpha)_\gamma \left[f_\alpha^{eq} + \left(1 - \frac{1}{2\tau}\right) f_\alpha^{neq} \right] = \rho \boldsymbol{u}\boldsymbol{u} + p\boldsymbol{I} - \left[\mu \left[\nabla \boldsymbol{u} + (\nabla \boldsymbol{u})^{\mathrm{T}}\right]\right], \tag{A4}$$

where $\boldsymbol{e}_\alpha$ is the lattice velocity vector along the α direction, τ is the single relaxation parameter, $\boldsymbol{I}$ is the second-rank unit tensor, f_α^{eq} is the equilibrium distribution function, and $f_\alpha^{neq} = -\tau \delta_t (\partial/\partial t + \boldsymbol{e}_\alpha \nabla) f_\alpha^{eq}$.

A.2. *Boundary-condition-enforced immersed boundary method*

Instead of applying complex body-fitted Eulerian meshes, the influence of the structure on the fluid is resolved by the boundary-condition-enforced immersed boundary method (Wu & Shu 2009; Wang *et al.* 2015), which gives

$$\boldsymbol{u}^{\boldsymbol{n+1}} = \boldsymbol{u}^* + \Delta \boldsymbol{u}, \tag{A5}$$

where $\boldsymbol{u}^*$ is the intermediate fluid velocity without considering the boundary effect (namely, the velocity field resolved by (A1) with $\boldsymbol{f} = 0$), $\boldsymbol{u}^{\boldsymbol{n+1}}$ is the velocity of the

https://doi.org/10.1017/jfm.2025.10590 Published online by Cambridge University Press

next step, and $\Delta \boldsymbol{u}$ is the correction velocity at each Eulerian mesh point. This can be approximated by interpolations using the velocity correction $\Delta \boldsymbol{u}_{\boldsymbol{B}}{}^{l}$ at the corresponding Lagrangian mesh points:

$$\Delta \boldsymbol{u}(\boldsymbol{r}_j) = \sum_l \Delta \boldsymbol{u}_B^l \, \Delta s^l \cdot D\left(\boldsymbol{r}_j \boldsymbol{X}_B^l\right), \quad l = 1, \ldots, N, \tag{A6}$$

where $D(\boldsymbol{r}_j \boldsymbol{X}_B^l)$ is a smooth delta function, and $\Delta \boldsymbol{u}_B^l \, \Delta s^l$ is dependent upon the accurate enforcement of the no-slip boundary condition on the Lagrange mesh points, which can be calculated by

$$\boldsymbol{A}\boldsymbol{X} = \boldsymbol{B}, \tag{A7}$$

where

$$\boldsymbol{X} = \left[\Delta \boldsymbol{u}_B^1 \, \Delta s^1, \Delta \boldsymbol{u}_B^2 \, \Delta s^2, \ldots, \Delta \boldsymbol{u}_B^N \Delta s^N\right]^{\mathrm{T}}, \tag{A8}$$

$$\boldsymbol{A} = h^2 \begin{pmatrix} D_{11} & D_{12} & \cdots & D_{1M} \\ D_{21} & D_{22} & \cdots & D_{2M} \\ \vdots & \vdots & \ddots & \vdots \\ D_{N1} & D_{N2} & \cdots & D_{NM} \end{pmatrix} \begin{pmatrix} D_{11}^B & D_{12}^B & \cdots & D_{1N}^B \\ D_{21}^B & D_{22}^B & \cdots & D_{2N}^B \\ \vdots & \vdots & \ddots & \vdots \\ D_{M1}^B & D_{M2}^B & \cdots & D_{MN}^B \end{pmatrix}, \tag{A9}$$

$$\boldsymbol{B} = \begin{pmatrix} \boldsymbol{U}_B^1 \\ \boldsymbol{U}_B^2 \\ \vdots \\ \boldsymbol{U}_B^N \end{pmatrix}^{n+1} - \begin{pmatrix} D_{11} & D_{12} & \cdots & D_{1M} \\ D_{21} & D_{22} & \cdots & D_{2M} \\ \vdots & \vdots & \ddots & \vdots \\ D_{N1} & D_{N2} & \cdots & D_{NM} \end{pmatrix} \begin{pmatrix} \boldsymbol{u}_1^* \\ \boldsymbol{u}_2^* \\ \vdots \\ \boldsymbol{u}_M^* \end{pmatrix}. \tag{A10}$$

Here, $D_{ij} = D(\boldsymbol{r}_j - \boldsymbol{X}_B^i)$ and $D_{ij}^B = D(\boldsymbol{r}_i - \boldsymbol{X}_B^j)$. After calculating $\Delta \boldsymbol{u}_B^l \, \Delta s^l$ at all Lagrange mesh points, the velocity correction is made at the Eulerian mesh points in (A5) and (A6). Furthermore, the forces and moments in (2.3) and (2.4) can be calculated by

$$\boldsymbol{F} = \left(F_X, F_Y\right) = -\sum_l \frac{\rho \Delta \boldsymbol{u}_B^l \Delta s^l}{\Delta t} + \rho V_B \frac{\mathrm{d}\boldsymbol{U}_B}{\mathrm{d}t}, \tag{A11}$$

$$T_Z = -\sum_l \frac{\rho_f \left(\boldsymbol{X}_B^l - \boldsymbol{X}_c\right) \times \left(\Delta \boldsymbol{u}_B^l \, \Delta s^l\right)}{\Delta t} + \frac{\rho_f}{\rho_s} \cdot I_B \cdot \frac{\mathrm{d}\omega}{\mathrm{d}t}, \tag{A12}$$

where $\boldsymbol{X}_B^l$ and $\boldsymbol{X}_c$ are the boundary point and the mass centre of the structure, and V_B is the volume of the structure. More details of the numerical method can be found in the literature (Wang *et al.* 2015, 2017; Qin, Yu & Wu 2024).

A.3. *The maximum Lyapunov exponent*

The maximum Lyapunov exponent is a quantitative measure used to assess the presence and the intensity of chaotic behaviour in a dynamical system. A positive value of the maximum Lyapunov exponent is a sign of chaos, and a larger positive value represents the degree of chaos of the system. The algorithm of Wolf *et al.* (1985) is widely used to estimate the Lyapunov exponent of a set of experimental or simulated time series data. The core idea of the algorithm is to track how small perturbations to the trajectory grow over time. For a scalar time series $X(t)$, the algorithm first reconstructs the phase space as

$$X(t) = [x(t), x(t+\tau), x(t+2\tau), \ldots, x(t+(m-1)\tau)], \tag{A13}$$

https://doi.org/10.1017/jfm.2025.10590 Published online by Cambridge University Press

where τ is the time delay, and m is the embedding dimension. The algorithm selects an initial point $X(t_0)$ first, and finds its nearest neighbour $X_0(t_0)$ in phase space. Then it tracks the evolution of both $X(t_i)$ and $X_0(t_i)$ over time until their separation $L(t_0) = |X_0(t_i) - X(t_i)|$ grows beyond a predefined threshold. At this point, a new neighbour is selected, and the process is repeated to continue the tracking until the end of the time series. Then the maximum Lyapunov exponent can be obtained by

$$\lambda_{max} = \frac{1}{t_n - t_0} \sum_{k}^{n} \ln \frac{L(t_k)}{L(t_0)}, \tag{A14}$$

where n is the total repeat number. In this work, the turn angle of the circular cylinder is selected for the time series data.

References

Andersen, A., Pesavento, U. & Wang, Z.J. 2005 Unsteady aerodynamics of fluttering and tumbling plates. *J. Fluid Mech.* **541**, 65–90.

Apelt, C.J., West, G.S. & Szewczyk, A.A. 1973 The effects of wake splitter plates on the flow past a circular cylinder in the range $10^4 < R < 5 \times 10^4$. *J. Fluid Mech.* **61** (1), 187–198.

Assi, G.R.S., Bearman, P.W. & Kitney, N. 2009 Low drag solutions for suppressing vortex-induced vibration of circular cylinders. *J. Fluids Struct.* **25** (4), 666–675.

Bagheri, S., Mazzino, A. & Bottaro, A. 2012 Spontaneous symmetry breaking of a hinged flapping filament generates lift. *Phys. Rev. Lett.* **109** (15), 154502.

Basso, R.L.G., Hwang, Y., Assi, G.R.S. & Sherwin, S.J. 2021 Instabilities and sensitivities in a flow over a rotationally flexible cylinder with a rigid splitter plate. *J. Fluid Mech.* **928**, A24.

Choi, H., Jeon, W.-P. & Kim, J. 2008 Control of flow over a bluff body. *Annu. Rev. Fluid Mech.* **40**, 113–139.

Choi, S., Lee, M., Roh, C. & Kim, D. 2025 Freely falling sphere with a rigid rear-side filament. *J. Fluid Mech.* **1010**, A43.

Cimbala, J.M. & Chen, K.T. 1994 Supercritical Reynolds number experiments on a freely rotatable cylinder/splitter plate body. *Phys. Fluids* **6** (7), 2440–2445.

Cimbala, J.M. & Garg, S. 1991 Flow in the wake of a freely rotatable cylinder with splitter plate. *AIAA J.* **29** (6), 1001–1003.

Cimbala, J.M. & Leon, J. 1996 Drag of freely rotatable cylinder/splitter-plate body at subcritical Reynolds number. *AIAA J.* **34** (11), 2446–2448.

Cummins, C., Seale, M., Macente, A., Certini, D., Mastropaolo, E., Viola, I.M. & Nakayama, N. 2018 A separated vortex ring underlies the flight of the dandelion. *Nature* **562** (7727), 414–418.

Favier, J., Dauptain, A., Basso, D. & Bottaro, A. 2009 Passive separation control using a self-adaptive hairy coating. *J. Fluid Mech.* **627**, 451–483.

Fish, F.E. & Lauder, G.V. 2006 Passive and active flow control by swimming fishes and mammals. *Annu. Rev. Fluid Mech.* **38**, 193–224.

Gu, F., Wang, J.S., Qiao, X.Q. & Huang, Z. 2012 Pressure distribution, fluctuating forces and vortex shedding behavior of circular cylinder with rotatable splitter plates. *J. Fluids Struct.* **28**, 263–278.

Horowitz, M. & Williamson, C.H.K. 2010 The effect of Reynolds number on the dynamics and wakes of freely rising and falling spheres. *J. Fluid Mech.* **651**, 251–294.

Huang, W.-X., Shin, S.J. & Sung, H.J. 2007 Simulation of flexible filaments in a uniform flow by the immersed boundary method. *J. Comput. Phys.* **226** (2), 2206–2228.

Jenny, M., Duek, J. & Bouchet, G. 2004 Instabilities and transition of a sphere falling or ascending freely in a Newtonian fluid. *J. Fluid Mech.* **508**, 201–239.

Jiang, H., Pfister, J.-L., Huang, D.Z. & Cao, S. 2025 Koopman reduced-order modeling and analysis of flag flapping in the wake of a cylinder. *Phys. Rev. E* **111**, 045101.

Kwon, K. & Choi, H. 1996 Control of laminar vortex shedding behind a circular cylinder using splitter plates. *Phys. Fluids* **8** (2), 479–486.

Lacis, U., Brosse, N., Ingremeau, F., Mazzino, A., Lundell, F., Kellay, H. & Bagheri, S. 2014 Passive appendages generate drift through symmetry breaking. *Nat. Commun.* **5**, 5310.

Lacis, U., Olivieri, S., Mazzino, A. & Bagheri, S. 2017 Passive control of a falling sphere by elliptic-shaped appendages. *Phys. Rev. Fluids* **2** (3), 033901.

Lentink, D., Dickson, W.B., Van Leeuwen, J.L. & Dickinson, M.H. 2009 Leading-edge vortices elevate lift of autorotating plant seeds. *Science* **324** (5933), 1438–1440.

https://doi.org/10.1017/jfm.2025.10590 Published online by Cambridge University Press

MUÑOZ-HERVÁS, J.C., LORITE-DÍEZ, M., RUIZ-RUS, J. & JIMÉNEZ-GONZÁLEZ, J.I. 2024 Experimental study on the flow-induced vibrations of a circular cylinder with a rear flexibly hinged splitter plate. *Phys. Fluids* **36** (2), 027106.

NAMKOONG, K., YOO, J.Y. & CHOI, H.G. 2008 Numerical analysis of two-dimensional motion of a freely falling circular cylinder in an infinite fluid. *J. Fluid Mech.* **604**, 33–53.

PENG, Z.-R., SUN, Y., YANG, D., XIONG, Y., WANG, LEI & WANG, L. 2022 Scaling laws for drag-to-thrust transition and propulsive performance in pitching flexible plates. *J. Fluid Mech.* **941**, R2.

QIN, J., YU, H. & WU, J. 2024 On the investigation of shock wave/boundary layer interaction with a high-order scheme based on lattice Boltzmann flux solver. *Adv. Aerodyn.* **6** (1), 6.

ROSHKO, A. 1954 On the drag and shedding frequency of two-dimensional bluff bodies. *NACA TN* 3169. Available at: https://ntrs.nasa.gov/citations/19930083869.

SEYED-AHMADI, A. & WACHS, A. 2019 Dynamics and wakes of freely settling and rising cubes. *Phys. Rev. Fluids* **4** (7), 074304.

SUN, X., SUH, C.S., YE, Z.-H. & YU, B. 2020 Dynamics of a circular cylinder with an attached splitter plate in laminar flow: a transition from vortex-induced vibration to galloping. *Phys. Fluids* **32** (2), 027104.

SUN, Y., PENG, Z.-R., YANG, D., XIONG, Y., WANG, L. & WANG, LIN 2022 Dynamics of a rigid-flexible coupling system in a uniform flow. *J. Fluid Mech.* **943**, A44.

TANG, T., ZHU, H., WANG, J., ALAM, M.M., SONG, J. & CHEN, Q. 2022 Flow-induced rotation modes and wake characteristics of a circular cylinder attached with a splitter plate at low Reynolds numbers. *Ocean Engng* **266**, 112823.

WANG, Y., SHU, C., TEO, C.J. & WU, J. 2015 An immersed boundary–lattice Boltzmann flux solver and its applications to fluid–structure interaction problems. *J. Fluids Struct.* **54**, 440–465.

WANG, Y., SHU, C., YANG, L.M. & SUN, Y. 2017 On the immersed boundary–lattice Boltzmann simulations of incompressible flows with freely moving objects. *Intl J. Numer. Meth. Fluids* **83** (4), 331–350.

WILLIAMSON, C.H.K. 1996 Vortex dynamics in the cylinder wake. *Annu. Rev. Fluid Mech.* **28**, 477–539.

WILLIAMSON, C.H.K. & BROWN, G.L. 1998 A series in $(1/\sqrt{Re})$ to represent the Strouhal–Reynolds number relationship of the cylinder wake. *J. Fluids Struct.* **12** (8), 1073–1085.

WOLF, A., SWIFT, J.B., SWINNEY, H.L. & VASTANO, J.A. 1985 Determining Lyapunov exponents from a time series. *Physica D* **16** (3), 285–317.

WU, J., QIU, Y.L., SHU, C. & ZHAO, N. 2014 Flow control of a circular cylinder by using an attached flexible filament. *Phys. Fluids* **26** (10), 103601.

WU, J. & SHU, C. 2009 Implicit velocity correction-based immersed boundary–lattice Boltzmann method and its applications. *J. Comput. Phys.* **228** (6), 1963–1979.

XU, J.C., SEN, M. & GAD-EL HAK, M. 1990 Low-Reynolds number flow over a rotatable cylinder–splitter plate body. *Phys. Fluids A* **2** (11), 1925–1927.

https://doi.org/10.1017/jfm.2025.10590 Published online by Cambridge University Press